THE ASEAN JOURNAL OF RADIOLOGY

September-December 2012
Volume XVIII Number III
ISSN 0859 144X

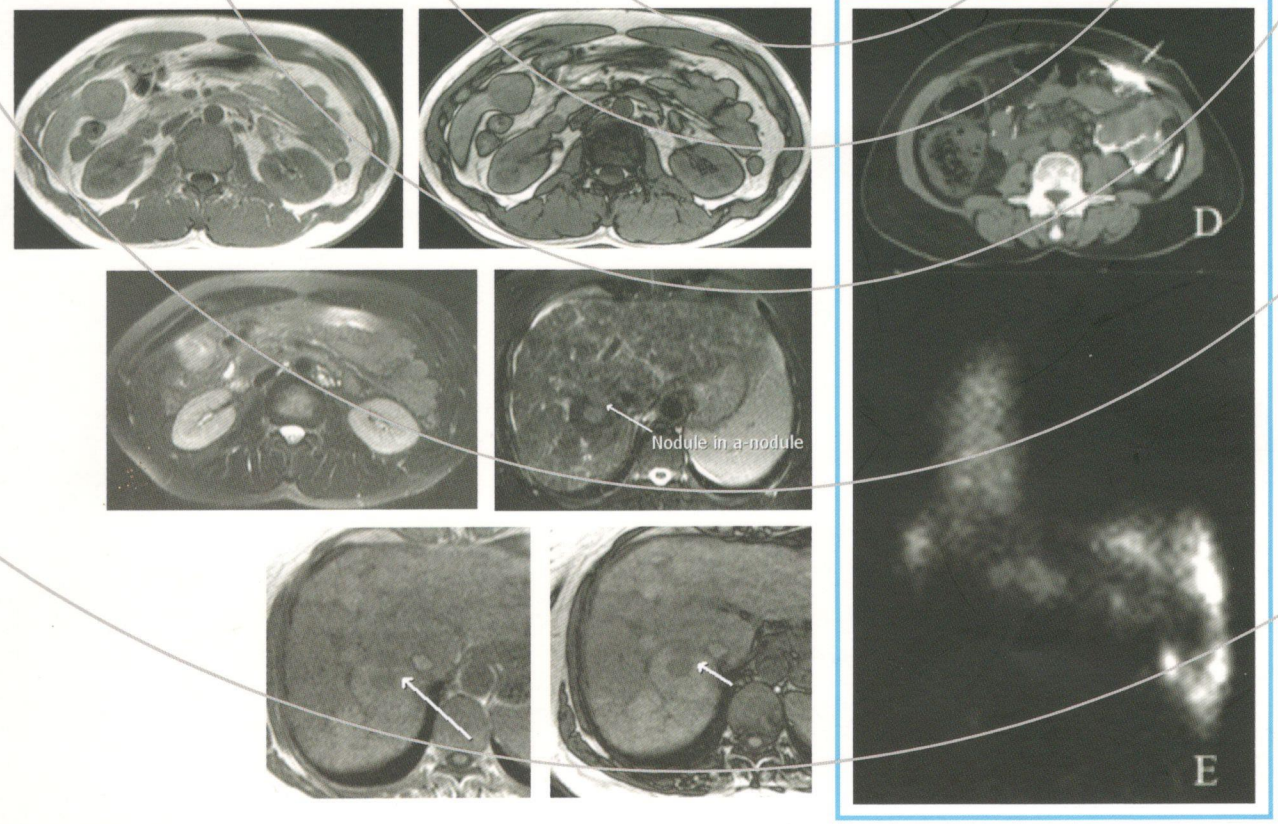

Published by

Royal College of Radiologists of Thailand

and

Radiological Society of Thailand

Bangkok, Thailand.

THE ASEAN JOURNAL OF RADIOLOGY
September-December 2012, Volume XVIII No.III

The Committee of Royal College of Radiologists of Thailand

Apr 2011-Mar 2013

President:	Permyot	Kosolbhand
Vice-president:	Sirintara	Singhara Na Ayudya
Secretariat General:	Pongdej	Pongsuwan
Vice-secretary General:	Alongkorn	Kiatdilokrath
Treasurer:	Krisdee	Prabhassawat
Academic president:	Anchalee	Churojana
House Master & Social Programme:	Kiat	Arjhansiri
Secretary:	Vithya	Varavithya
Registrar:	Pisit	Wattanaruangkowit
Committee:	Poonsook	Jitnuson
	Chamaree	Chuapatcharasopon
	Chantima	Rongviriyapanich
	Nitra	Piyaviseipat

The Committee of Radiological Society of Thailand

Apr 2011-Mar 2013

President:	Permyot	Kosolbhand
Vice-president:	Sirintara	Singhara Na Ayudya
Secretariat General:	Pongdej	Pongsuwan
Treasurer:	Krisdee	Prabhassawat
Academic president:	Anchalee	Churojana
House Master&Social Programme:	Kiat	Arjhansiri
Committee:	Poonsook	Jitnuson
	Chamaree	Chuapatcharasopon
	Chantima	Rongviriyapanich
	Nitra	Piyaviseipat
	Amphai	Uraiverotchanakorn

The Journal of the Royal College of Radiologists & Radiological Society of Thailand

(2011 - 2013)

Office:

1. Department of Radiology, Faculty of medicine, Ramathibodi hospital 270, Rama VI Road, Toong Phayathai, Ratchathewi, Bangkok, 10400
Tel 02-2011259#110, Fax 02-2011297
E-mail Sirintarapongpech2@hotmail.com

2. The Royal college of Radiologists & Radiological society of Thailand. 9th Floor, Royal Golden Jubilee Building, 2 Soi Soonvijai, Petchburi Road, Bankok, 10320
Tel 02-7165963, Fax 02-7165964
E-mail rcrtthailand@gmail.com

Contents

Original Article

Case Report

THE ASEAN JOURNAL OF RADIOLOGY 2012: 18(3): 137-144 137

Original Article

Pilot Study: A Comparison of Dose Distribution between 3-Dimensional Conformal and Intensity Modulated Radiation Therapy for Craniospinal Irradiation in Medulloblastoma.

Suntornpong N, MD., Tuntipumiamorn L, M.Sc. (Radiological science), Iampongpaiboon P, M.Sc. (Medical physics), Liammookda P, M.Sc. (Medical physics)

Division of Radiation Oncology, Department of Radiology, Faculty of Medicine Siriraj Hospital, Mahidol University, Bangkok 10700, Thailand

Abstract

Objectives: To evaluate and compare the results of dose distribution in terms of target coverage and normal tissue sparing for 3 RT techniques including 3-dimensional conformal radiation therapy (3DCRT), field in field intensity modulated radiation therapy (FIF) and intensity modulated radiation therapy (IMRT) in spinal axis from craniospinal irradiation (CSI).

Methods and materials: Ten patients with medulloblastoma were included in this study. Planning CT simulation were performed in supine position with customized thermoplastic mask on head rest set. Treatment planning for each patients were performed in 3 separate techniques : 3DCRT, FIF and IMRT.

Results: Three techniques showed a comparable the volume of planning target volume receiving at least 95% of the prescribed dose (PTV95%). Significant differences between 3 techniques were found for the volume of planning target volume receiving at least 107% of the prescribed dose (PTV107%) with the lowest result in IMRT.

The volume receiving intermediate dose 10 Gy(V10), high dose 20 Gy(V20) and the maximum dose percentage of prescribed dose (Dmax) in IMRT were lower than that in 3DCRT and FIF in all OARs. In contrast, the volume receiving low dose 3 Gy(V3) from IMRT was higher to that of 3DCRT and FIF in all OARs.

Conclusion: IMRT is one of the effective advanced radiation therapy technique for CSI in regard to homogeneous dose in target coverage and minimized radiation dose to organ at risk.

Keywords: 3-dimensional conformal radiation therapy, intensity modulated radiation therapy, craniospinal irradiation, medulloblastoma

Introduction

Medulloblastoma is one of pediatric brain tumor that has spreading propensity to entire craniospinal axis. Current treatment modalities include combination of surgery, chemotherapy and radiation therapy (RT). Craniospinal irradiation (CSI) is the standard volume for RT in this disease. This radiation treatment is one of the most technically challenging because of the need of homogeneous dose distribution in complex shaped target volume especially at craniospinal and spinal-spinal junction. Additionally, several long-term treatment-related side effects from CSI have to be concerned in pediatric patients. These include neurocognitive and neuro-endocrine deficits, cardiac dysfunction, pulmonary disease, infertility and secondary malignancies. Recently, computed tomography-based treatment planning and delivery for CSI has been developed to improve target homogeneity and sparing of organs at risk. These various radiation techniques include 3-dimensional conformal RT (3DCRT), intensity modulated RT (IMRT), volumetric arc RT (VMAT) and helical tomotherapy.

The goal of this study is to evaluate and compare the results of dose distribution in terms of target coverage and normal tissue sparing for 3 RT techniques including 3DCRT, FIF and IMRT in spinal axis from CSI.

Methods and materials

Ten patients (age, range 5-13 years, mean 7 years) with medulloblastoma previously treated with 3DCRT for CSI were included in this study. Planning CT simulation were performed in supine position with customized thermoplastic mask on head rest set. The CT axial images were obtained from vertex to coccyx with 3 mm contiguous slice thickness. CT datasets were tranfered to treatment planning system (Eclipse version 8.1 Varian Medical System, Palo Alto, CA)

The clinical target volume (CTV) of brain included entire brain and meninges. The CTV of spine covered entire spinal canal including cerebrospinal extension to spinal ganglia. The planning target volume (PTV) of brain and spine included 5 mm margin in all directions of CTV. Organ at risks (OARs) consisted of thyroid, lungs, heart, liver and kidneys. This study was approved by Siriraj Ethical Committee (Si 461/2008)

Treatment planning

Treatment planning for each patients were performed in 3 separate techniques: 3DCRT, FIF and IMRT. With 6-MV photon, dose 23.4 Gy in 13 fractions (1.8Gy per fraction) to craniospinal axis was prescribed for all patients.

All plans used lateral opposed fields for brain with half beam block technique.

For 3DCRT planning ,a direct posterior field was used to treat spine. The isocenter was located at the level of C2-C4 which based on anatomy of the patients for brain field and at the level of T10-T12 with fixed distance of 20 cm from brain isocenter for spine fields.If spinal length was exceed than 40 cm, the second spine isocenter was placed at the level of S2-S3. The isocenter placements were set as a reference for the entire of treatment course and longitudinal shift is designed for the isocenters shift. The collimator was rotated for the brain field to match the divergence of spine field.The moving gap junction technique between 2 spine fields using asymmetric field was proposed as shown

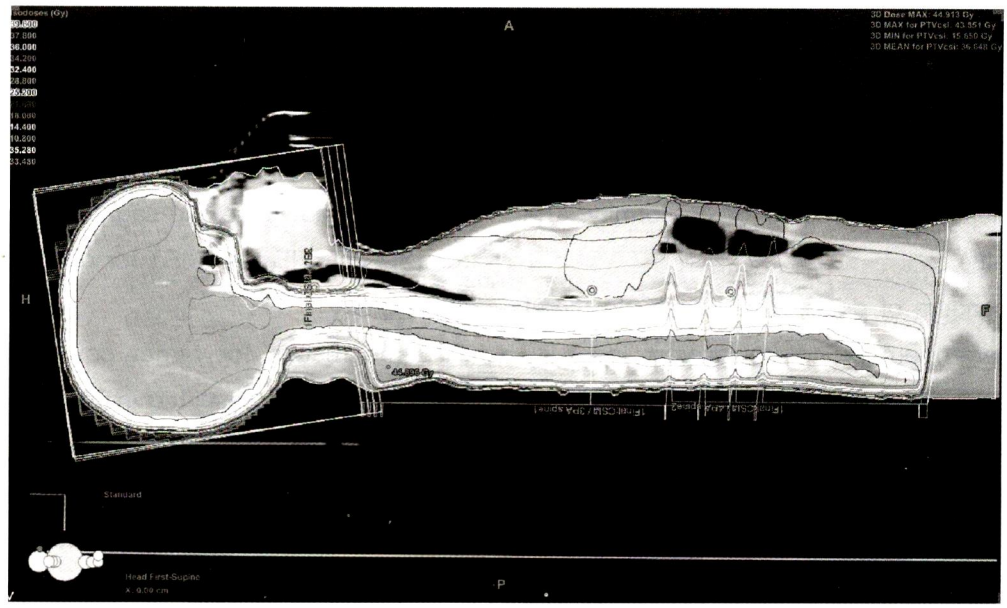

Fig.1 Isodose coverage of PTV in 3DCRT planning. The shifts of junctions and gaps between fields were shifted daily from caudal-cranial direction.

in Figure 1. Beam weighting was adjusted to ensure the dose of PTV has covered within 95% isodose curve.

For FIF planning, field arrangement and isocenters were set in the same location as 3DCRT planning. Multiple lower-weighting reduction fields was used for PTV spine planning. The reduction field contained shielded segment with small weighting to conform the dose at the concaved and elongated target. The minimal number of fields with the field-in-field technique is 4-10, depending on the complexity of plan. The 95% isodose lines coverage to PTV were obtained by segmented field. The field-in-field plan was attained an automatically modulated dose at the gap and junctions that eliminated intrafractional junction shift.

For IMRT planning, 5 posterior fileds by inverse planning and dynamic multileaf collimator-based technique were generated with gantry angle at 140, 160, 180, 200 and 220 degree. The optimization was done to spare OARs as much as possible with optimum target coverage.

Plan evaluation

The treatment plans of 3 techniques were compared in terms of target coverage and homogeneity and OARs sparing in spinal axis RT.

Spinal PTV coverage were assessed as the volume of PTV receiving at least 95% and at least 107% of the prescribed dose (PTV95% and PTV 107% respectively). The maximum dose percentage of precscribed dose (Dmax) were also evaluated. The dose homogeneity were determined by homogeneity index (HI), Conformation number (CN) and Inhomogeneity coefficient (IC) as follows.[1-3]

HI = (Dmax-Dmin)/prescribed dose

CN = (PTV95%/PTV) x (PTV95%/vol of 95%)

IC1 = (d2%-D98%)/Dmean

IC2-(d5%-D95%)/D mean

HI measure the difference between maximum dose and minimum dose in PTV to the prescribed dose.

CN measure the degree of conformity. The optimum value is 1.

IC measure of dose nonuniformity in target volume. A large number indicate greater variability target dose.

For each OARs, the dose was evaluated as the volume of each organ receiving at least 3Gy, 10Gy and 20 Gy (V3, V10 and V20 respectively)

Statistical analysis

Repeated measure ANOVA and Friedman test with multiple comparisons test by Bonferroni correction were used to determine statistical significance.

Results

Fig 2 shows the mid-sagittal dose distribution from 3DCRT, FIF and IMRT for one of the patients in this study.

The results for target coverage and dose homogeneity are presented in Table 1. Three techniques showed a comparable PTV95%. Significant differences between 3 techniques were found for PTV107% with the lowest result in IMRT.

IMRT showed the highest HI which was significant different to that of FIF. CN were comparable in all 3 techniques. IC2 was highest in 3DCRT which was significant different to that of IMRT.

Fig 2. Mid-sagittal dose distribution from 3DCRT, FIF and IMRT

Table 1 Target coverage and dose homogeneity

PTVCSI	3D	FIF	IMRT	p-value[#]
PTV95%	97.3 ± 1.9	94.9 ± 4.5	96.1 ± 2.2	0.062
PTV107%	18.9 ± 11.7	12.5 ± 8.1	1.2 ± 0.9	< 0.001[a,b]
PTV110%	7.0 ± 5.2	6.1 ± 4.7	0.3 ± 0.1	0.002[a,b]
PTVDmax	27.2 ± 0.8	27.2 ± 1.4	30.5 ± 1.9	< 0.001[a,b]
PTVDmax	116.4 ± 3.2	116.2 ± 6.2	130.4 ± 8.3	< 0.001[a,b]
HI	0.85 ± 0.30	0.79 ± 0.28	0.97 ± 0.25	0.009[b]
CN	0.70 ± 0.07	0.70 ± 0.07	0.70 ± 0.22	1.000
IC1	0.17 ± 0.04	0.17 ± 0.05	0.14 ± 0.05	0.097
IC2	0.10 ± 0.02	0.09 ± 0.03	0.08 ± 0.02	0.044[a]

Data expressed as mean ± SD.

[#] Repeated measures ANOVA and Friedman test with multiple comparisons test by Bonferroni correction.

[a] Statistical significance between 3D versus IMRT.

[b] Statistical significance between FIF versus IMRT.

The results for percentage volume of each OARs from 3 techniques are shown in Table 2.

The volume receiving intermediate dose (V10), high dose (V20) and Dmax in IMRT were lower than that in 3DCRT and FIF in all OARs. These difference were statistical significant for V10 in heart, liver and right kidney and V20 in thyroid. The high dose volume (V20) were almost negligible for all OARs from IMRT. In contrast, the low dose volume (V3) from IMRT was higher to that of 3DCRT and FIF in all OARs. These difference were statistical significant in all organs except thyroid.

Discussion

The goal of CSI is to deliver homogeneous dose for target coverage while minimizing radiation dose to organ at risk. Traditionally, CSI was done with patients in prone position which cause several aspects to be concerned include immobilization, set up reproducibility and airway access for pediatric anesthesia. Various novel RT technique with supine position have been studies to overcome these limitation.

In this study, all 3 techniques yielded comparable spinal target coverage in term of PTV95%. While PTV107% was highest in 3DCRT due to geometrically complex in spinal PTV. This result correlated to a report by Parker et al which standard 2D, 3D and 5-field inverse planned IMRT technique were compared for spinal axis irradiation[4].

Panandiker et al also reported result compared posteroanterior IMRT to standard posterior technique to spinal field. They showed significant improvement in target coverage with 8% increased PTV95% and 7% decreased PTV more than 110% in IMRT[5]

For dose homogeneity,this study showed the highest HI in IMRT while IC which measure dose nonuniformity was highest in 3DCRT. In a report by Studenski et al, IMRT homogeneity was also significantly better than for 3DCRT plan[6].

Sharma et al evaluated 3DCRT, IMRT and helical tomotherapy, they showed improved dose homogeneity by 5 field inversely planned IMRT for spinal target volume compared to 3DCRT. The highest dose heterogeneity in 3DCRT was due to

Table 2 Percentage volume of each OARs

OAR	3D	FIF	IMRT	p-value[#]
Thyroid				
V3	96.4 ± 11.3	91.8 ± 20.4	98.6 ± 2.5	0.516
V10	85.9 ± 26.8	70.6 ± 27.7	65.5 ± 20.5	0.092
V20	6.0 (0, 44)	4.8 (0, 50.8)	0 (0, 2.3)	0.009[b,c]
Dmax	20.5 ± 1.8	21.1 ± 1.0	18.0 ± 2.2	< 0.001[b,c]
Dmean	16.2 ± 4.2	14.9 ± 3.6	10.7 ± 1.7	< 0.001[b,c]
Dmin	6.3 (2, 18)	3.1 (2.1, 18.4)	3.0 (2.4, 9.9)	0.122
Rt lung				
V3	19.3 ± 4.5	20.4 ± 5.3	60.8 ± 5.2	< 0.001[b,c]
V10	10.9 ± 3.9	10.9 ± 4.0	9.2 ± 3.7	0.443
V20	4.8 (0.8, 24.7)	4.0 (0.3, 16.8)	0.1 (0, 24.2)	0.202
Dmax	23.3 ± 0.8	22.8 ± 0.8	21.4 ± 1.7	0.001[b,c]
Dmean	3.0 ± 0.7	3.1 ± 0.7	4.6 ± 0.5	< 0.001[b,c]
Dmin	0.26 ± 0.03	0.29 ± 0.09	0.44 ± 0.07	< 0.001
Lt lung				
V3	9.4 ± 4.3	10.0 ± 4.8	49.5 ± 6.5	< 0.001[b,c]
V10	4.2 ± 2.7	4.2 ± 2.7	3.9 ± 1.8	0.836
V20	0.70 (0, 2.3)	0.70 (0, 11.7)	0.03 (0, 23.9)	0.368
Dmax	22.6 ± 1.6	22.4 ± 1.5	21.0 ± 3.2	0.076
Dmean	1.7 ± 0.6	1.8 ± 0.6	3.8 ± 0.5	< 0.001[b,c]
Dmin	0.26 ± 0.04	0.28 ± 0.05	0.63 ± 0.31	< 0.001[b,c]
Heart				
V3	70.2 ± 11.0	69.9 ± 11.1	95.1 ± 11.7	0.005[b,c]
V10	54.9 ± 16.1	59.7 ± 10.6	15.3 ± 12.9	< 0.001[b,c]
V20	4.8 (0.8, 18.4)	1.3 (0.02, 74.9)	0 (0, 64.7)	0.285
Dmax	21.8 ± 0.9	21.3 ± 0.8	17.0 ± 1.6	< 0.001[b,c]
Dmean	11.3 ± 1.8	10.6 ± 2.7	6.8 ± 1.5	< 0.001[b,c]
Dmin	0.64 ± 0.15	0.64 ± 0.25	2.24 ± 0.71	< 0.001[b,c]
Liver				
V3	33.5 ± 17.7	28.3 ± 4.8	47.1 ± 10.9	< 0.001[c]
V10	27.2 ± 15.2	22.6 ± 4.2	3.0 ± 1.5	< 0.001[b,c]
V20	0.6 (0, 18.5)	0.5 (0, 29.9)	0 (0, 24.5)	0.332
Dmax	21.8 ± 1.2	21.4 ± 0.9	17.1 ± 2.4	0.001[b,c]
Dmean	4.5 ± 0.7	4.5 ± 0.7	3.4 ± 0.6	< 0.001[b,c]
Dmin	0.16 ± 0.06	0.20 ± 0.05	0.31 ± 0.06	< 0.001[b,c]

Table 2 Percentage volume of each OARs *(Cont.)*

OAR	3D	FIF	IMRT	p-value#
Rt kidney				
V3	12.2 ± 6.9	12.9 ± 7.1	29.2 ± 11.9	< 0.001[b,c]
V10	4.5 ± 4.0	4.8 ± 4.2	1.3 ± 1.4	0.048[b,c]
V20	0.02 (0, 3.35)	0.32 (0, 10.9)	0 (0, 22.5)	0.291
Dmax	19.9 ± 3.4	20.8 ± 4.6	12.9 ± 4.7	0.001[b,c]
Dmean	1.9 ± 0.8	2.1 ± 0.9	2.6 ± 0.6	0.001[a,b,c]
Dmin	0.30 ± 0.05	0.35 ± 0.11	0.63 ± 0.17	0.002[b,c]
Lt kidney				
V3	11.0 ± 5.9	11.2 ± 5.9	36.8 ± 9.2	< 0.001[b,c]
V10	4.6 ± 3.6	4.7 ± 3.8	2.8 ± 1.5	0.297
V20	0.4 (0, 3.5)	1.3 (0, 13.1)	0 (0, 24.6)	0.381
Dmax	20.9 ± 2.3	21.7 ± 3.5	17.0 ± 2.7	< 0.001[b,c]
Dmean	1.8 ± 0.7	1.9 ± 0.9	3.1 ± 0.5	< 0.001[b,c]
Dmin	0.26 ± 0.05	0.31 ± 0.09	0.59 ± 0.09	< 0.001[b,c]

Data expressed as mean ± SD

Repeated measures ANOVA and Friedman test with multiple comparisons test by Bonferroni correction.

[a] Statistical significance between 3D versus FIF.

[b] Statistical significance between 3D versus IMRT.

[c] Statistical significance between FIF versus IMRT.

single direct posterior field for contour irregularity in spinal axis[7].

For OAR sparing, this study showed that IMRT were superior to 3DCRT and FIF while 3DCRT and FIF yield similar results. Reduction dose to lung by IMRT should minimize acute pulmonary side effect. IMRT is also expected to reduce late toxicities such as cardiac dysfunction in this study. The concern regarding late treatment-related toxicities is significant in medulloblastoma due to approaching cure rate to 70% from current combined modality treatment.

Another concern of IMRT in pediatric cancer is carcinogenic risk. This technique provides low radiation dose to larger volume of normal tissue compare to that from 3DCRT and FIF technique in this study. Carcinogenicity from radiation is high for tissues receiving low dose. Radiation-induced carcinoma may develop from much lower dose than radiation-induced sarcoma.[8] Although second malignancy is an uncommon but it is one of the lifethreatening complication of RT.

References

1. Optimal normal tissue sparing in craniospinal axis irradiation using IMRT with daily intrafractionally modulated junctions. Kusters JM, Louwe RJ, van Kollenburg PG, Kunze-Busch MC, Gidding CE, van Lindert E et al. Int J Radiat Oncol boil Phys 2011;81:1405-14.
2. Improving cardiac dosimetry : alternative beam arrangements for intensity modulated radiation therapy planning in patients with carcinoma of the distal esophagus. Grosshans D, Boehling NS, Palmer M, Spicer C, Erice R, Cox JD et al. Practical Radiation Oncology 2012;2:41-5.
3. A conformation number to quantify the degree of con-formality in brachytherapy and external beam

irradiation: application to the prostate. van't Riet A, Mak AC, Moerland MA Elders LH, van der Zee W. Int J Radiat Oncol Bioll Phys 1997;37:731-6.

4. High-precision radiotherapy for craniospinal irradiation: evaluation of three-dimensional conformal radiotherapy, intensity-modulated radiation therapy and helical TomoTherapy. Parker W, Filion E, Roberge D, Freeman CR. Int J Radiat Oncol Biol Phys 2007;69:251-7.
5. Craniospinal irradiation with spinal IMRT to improve target homogeneity. Pai Panandiker A, Ning H, Likhacheva A, Ullman K, Arora B, Ondos J et al.Int J Radiat Oncol Biol Phys 2007;68:1402-9
6. Intensity-modulated radiation therapy and volumetric-modulated arc therapy for adult craniospinal irradiation-A comparison with traditional techniques. Studenski MT, Shen X, Yu Y, Xiao Y, Shi W, Biswas Tet al. Med Dosim 2012;7
7. High-precision radiotherapy for craniospinal irradiation: evaluation of three-dimensional conformal radiotherapy, intensity-modulated radiation therapy and helical TomoTherapy. Sharma DS, Gupta T, Jalali R, Master Z, Phurailatpam RD, Sarin R. Br J Radiol 2009;82:1000-9
8. The effect of intensity modulated radiotherapy on radiation-induced second malignancies. Ruben JD, Davis S, Evans C, Jones P, Gagliardi F, Haynes M et al. Int J Radiat Oncol boil Phys 2008;70:1530-6.

THE ASEAN JOURNAL OF RADIOLOGY 2012: 18(3): 145-150 145

Original Article

Evaluation of Hepatic Hydrothorax by ^{99m}Tc-MAA Peritoneal Scintigraphy

Araya Boonyaleepan, MD.

Nuclear Medicine section, Department of Nuclear Medicine, Rajavithi Hospital

Abstract

Background: Hepatic hydrothorax occurs 6-10% of advance cirrhotic patient. If we can diagnose quickly and accurately, it can prevent the patients from unnecessary investigations and early start correct treatment.

Objective: To evaluate the results of using ^{99m}Tc-MAA peritoneal scintigraphy for demonstrate perito-neopleural communication in the patients with suspected hepatic hydrothorax.

Material and Method: Descriptive retrospective study. Collected and analized data of the cirrhotic patients who was investigated by ^{99m}Tc-MAA peritoneal scintigraphy in nuclear medicine section, Rajavithi hospital, Thailand from 2005-2012.

Results: Eleven patients were identified, 7 male and 4 female average age 52.55 years. Most common cause of cirrhosis was viral hepatitis C (45%) and almost all (10/11) were in child class C. 88% of patients who were evaluated by gastroscope had esophageal varies. 91% of patients had ascites which 90% were massive, 20% moderate and 10% small amount. Peritoneal scintigraphy were positive in 7 patients, excluded a patient who was suspected cause of pleural effusion form pulmonary infection, percent of demonstrated peritoneo-pleural communication was 70. A patient who didn't have ascites also had positive scintigraphy. Time since radiotracer administration until it appeared in pleural cavity was less than 1 hour in 57% of patients, 2 hours 14.3%, 4 hours 14.3% and 24 hours 14.3%.

Conclusion: ^{99m}Tc-MAA peritoneal scintigraphy is a safe, rapid, cheap, minimally invasive and low radiation method for evaluation of the patients who was suspected hepatic hydrothorax with medium positive results (70%) and high specificity.

Keywords: Hepatic hydrothorax, ^{99m}Tc-MAA, peritoneal scintigraphy

Introduction

Hepatic hydrothorax is explained in detail as the presence of more than 50 ml. pleural effusion in cirrhotic patients without primary lung or heart disease[1-5]. This condition occurs in approximately 6-10% of patients with advance cirrhosis[6,7] and it is thought to be 1%-2% of all pleural effusion[1,8,9]. The incidence of a pleural effusion in cirrhotic patients is much higher with the concomitant presence of ascites fluid.

Although the exact mechanism of hepatic hydrothorax is controversial but the most plausible etiology is direct passage of the ascites fluid in to the pleural space via defects in the diaphragm[1,20].

A rapid and simple method for evaluation of communication between peritoneal and pleural space is peritoneal scintigraphy. Peritoneal scintography is nuclear scan that can be performed by intraperitoneal administration of radiolabled tracer such as ^{99m}Tc-sulfur collid, ^{99m}Tc- human serum albumin, ^{99m}Tc-macroaggregated albumin (MAA). Later scintigraphic images of thoraco-abdominal region are performed by Gamma camera. The migration of radioisotopes from the peritoneal cavity in to pleural space confirms the presence of a communication.

Material and Method

The study is descriptive retrospective study. Collected and analized data of the cirrhotic patients with clinically suspected hepatic hydrothorax who was investigated by ^{99m}Tc-MAA peritoneal scintigraphy in nuclear medicine section, Rajavithi hospital, Thailand, from 2005-2012.

Peritoneal scintigraphic protocol:

1. Injection of ^{99m}Tc-MAA 5 mCi into peritoneal cavity by paracentesis.

2. Image acquisition by GE MPR single-head gamma camera, energy setting

140 keV ± 10% window.

2.1 dynamic 1 hour (60 sec./frame, total 60 frames)

Matrix size 128x128, low energy general purpose collimator (LEGP)

zoom 1.0, anterior view, FOV included chest and upper abdomen.

2.2 delay images: preset count 1000 kc.

Matrix size 256x256, LEGP anterior view. delay image every hour or as requested.

Extra views such as RAO, LAO as requested.

2.3 delay images till 24 hours after the tracer injection are obtained in the patients without radiotracer accumulation in pleural space during the first 6 hours.

Results

Eleven patients were included. Data considering age, gender, etiology of cirrhosis, Child classification, serum albumin, presence or absence of esophageal varices and complication or associated disease of all patients are present in table 1.

Data considering ascites, pleural effusion, findings of peritoneal scintigraphy and time from tracer administration until positive scan are shown in table 2.

All 11 patients were 7 male and 4 female. Average age was 52.55 years (18-78 yr.). The most common etiology of cirrhosis in this study was viral hepatitis C (45%), followed by alcohol (36%), viral hepatitis B (27%), autoimmune (9%) and unknown etiology (9%).

Ten patients (91%) were in Child class C. Serum albumin was 1.2-3 g/dL. Eight patients were

evaluated by gastroscope, 7 in 8 (88%) had esophageal varices. Four patients had clinical of GI bleeding. There are 2 patients had hepatomas and 1 patient was suspected.

Ten patients (91%) had ascites. Seven from ten (70%) had massive ascites, 20% had moderate ascites and 10% had minimal ascites. One patient didn't have ascites (by ultrasonography and CT scan).

The pleural effusion (by CXR) was on the right 8/11 (73%), left 3/11 (27%). Six patients had the results of pleural effusion analysis, 5 were transudate, 1 was exudate.

There was compatibility between CXR and scintigraphic results in 7 patients (63.64%). However if exclude a patient with negative scan who had exudative pleural effusion and right middle lung infiltration from CXR (because pleural effusion may be from pulmonary infection), the positive result will increase to be 70% (7 in 10 patients). Time since radiotracer administration until positive scan is less than 1 hour in 4 patients (57%), 2 hours 1 case (14.3%), 4 hours 1 case and 24 hours 1 case.

From all of scan positive patients, there were 5 positive on right side (71%), 2 positive on left side (29%)

All of scan result negative patients (4) had

Table 1 Information of the cirrhotic patients.

No	age	sex	cause of cirrhosis	child	serum albumin	Esophageal varices	Complication/ Associated disease
1	59	m	Viral hepatitis B	C	2.3	NE	Hepatocellular carcinoma
2	74	f	unknown	B	3	present	UGI bleed (DU & erosive gastritis), CKD, DM, HT
3	45	m	Alcoholic, Viral hepatitis C	C	2.1	NE	Acute renal failure, Spontaneous bacterial peritonitis
4	54	m	Alcoholic, Heptitis B virus carrier	C	2.5	NE	End stage renal disease (from Membranoproliferative glomerulonephritis)
5	44	m	Alcoholic	C	1.2	absent	
6	40	m	Alcoholic, Viral hepatitis B	C	2.4	present	UGIB (mucosal tear at EG junction), hepatic encephalopathy
7	65	f	Viral hepatitis C	C	1.7	present	Spontaneous bacterial peritonitis
8	18	m	AIH+PSC	C	2.1	present	LGIB (5colonic polyps), Spontaneous bacterial peritonitis
9	44	f	Viral hepatitis C	C	2.7	present	R/O small hepatocellular carcinoma 1 cm.
10	57	m	Viral hepatitis C	C	2.6	present	Hepatocellular carcinoma, UGIB
11	78	f	Viral hepatitis C	C	2.4	present	UGIB, erosive gastritis, DU, DM

AIH = autoimmune hepatitis, PSC = primary sclerosing cholangitis, NE = non evaluated, CKD = chronic kidney disease, UGIB = upper gastrointestinal bleeding, LGIB = lower gastrointestinal bleeding, DU = duodenal ulcer

Table 2 Information of ascites, pleural effusion and scintigraphic findings.

No	ascites	pleural effusion on CXR (amount/side)	pleural tapping	Scan findings	time of positive (hours)
1	medium positive	massive right	transudate	positive right	less than 1
2	minimal positive	massive right	NE	positive right	less than 2
3	massive positive	modearte left	NE	positive left	4
4	massive positive	moderate right	transudate	negative	
5	massive positive	massive right	NE	negative	
6	medium positive	massive right	NE	positive right	less than 1
7	massive positive	massive right	transudate	positive right	less than 1
8	massive positive	minimal right, minimal infiltration in RML	exudate	negative	
9	negative	moderate right	NE	positive right	less than 1
10	massive positive	small left	transudate	negative	
11	massive positive	massive left	transudate	positive left	24

massive ascites. Three had right pleural effusion on CXR, the other had on the left. Two had small amount of effusion, one had moderate and one had massive effusion.

Discussion

Emerson was the first who describe the diaphragmatic defects (post-mortem) in a patient with hepatic hydrothorax in 1955. These defects can be demonstrated not only grossly, but also microscopically in these patients[17]. These defects may also be visualized using thoracoscopy[13,18,19].

Microscopic examinations of these defects have revealed discontinuities or gaps in the collagen bundles that make up the tendinous portion of the diaphragm. When ascitic fluid collects within the peritoneal cavity, it raises the intra-abdominal pressure and tends to stretch the diaphragm, creating or enlarging these microscopic defects. Then herniation of peritoneum through these gaps into the pleural cavity can be occurred. This leads to the formation of pleuro-peritoneal blebs. These blebs are typically less than 1 cm. in diameter and tend to rupture, thus providing free communication between the peritoneal and pleural cavities. These blebs tend to occur more commonly in the right hemidiaphragm, may be related to embryonic development, the left hemidiaphragm is more muscular and relatively resistant to bleb formation[6,13]. The fluid in peritoneal cavity will be passed into pleural space via these blebs by negative intrathoracic pressure.

Lieberman FL et al, study 330 patients with cirrhosis and ascites, 6% also had a pleural effusion[1,10]. In another study, Johnston et al reported that 6% of 200 patients with cirrhosis had a pleural effusion but none of 54 without ascites had demonstrable pleural fluid[1,11]. However absence of ascites cannot exclude the cirrhotic etiology of pleural

effusion[12].

Regarding the reported case of hepatic hydrothorax, 85% have been right sided, 13% left sided and 2% bilateral[13]. But Alberts WM et al reported bilateral pleural effusion up to 15-30%[14].

The effusion is transudative but the protein content of the pleural effusion is usually slightly higher than that of ascitic fluid since the pleura has a higher absorptive capacity[14].

There are many diagnostic modalities to prove peritoneo-pleural communication included injection of air, contrast agents or radiopharmaceutical in to peritoneal cavity, MRI and surgical exploration by thoracoscopy[20].

We used ^{99m}Tc-MAA peritoneal scintigraphy for evaluation of communication between peritoneal and pleural spaces because it is a safe, rapid, cheap, minimally invasive method and low radiation to the patient. In a case without ascites we performed abdominal tapping under CT guide and introduction of 500 ml. 0.9% NSS in to peritoneal cavity before injection of ^{99m}Tc-MAA 5 mCi. as shown in Figure 1.

The peritoneal scintigraphy has been consi-

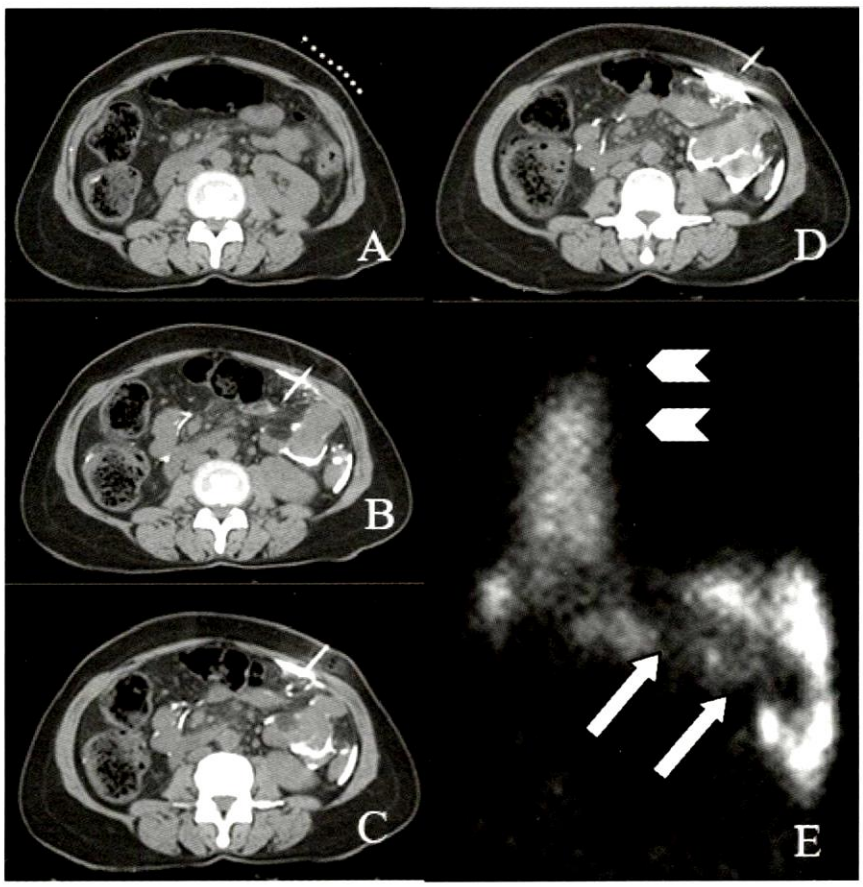

Fig.1 (A-D) CT scan images show CT guided abdominal tapping in a patient without ascites. Small amount of contrast media was injected to test position of the needle and (E) a ^{99m}Tc-MAA peritoneal scintigraphic image shows radiotracer activity in upper abdomen (arrows) and tracer migration into right sided pleural cavity (arrow heads), confirm condition of hepatic hydrothorax.

dered the "gold standard" for identification of hepatic hydrothorax because of very high specificity (upto 100%) and its sensitivity is about 71%. However its sensitivity can be improved by performing a thoracocentesis before administration of radiopharmaceutical in order to reduce pressure in pleural cavity[6].

Demonstration of peritoneo-pleural communication is importance in patient management because it can prevent unnecessary investigation and cause start correct treatment quickly.

Conclusion

^{99m}Tc-MAA peritoneal scintigraphy can be used for demonstrate peritoneo-pleural communication in cases of hepatic hydrothorax even if in case of absent ascites with fair sensitivity and very good specificity.

References

1. LS., Pinto, C. Maliska, ME Penas, LMB Fonseca. Radionuclide Evaluation of Hepatic Hydrothorax. Alasbimn Journal 2005;29
2. Lieberman FL, Hidemura R, Peters RL and Reynolds TB Pathogenesis and treatment of hydrothorax complication cirrhosis with ascites. Ann Intern. Med 1966:64:341-51
3. Lazaridis KN, Frank JW, Krowka M and Kamath PS. Hepatic hydrothorax: Pathogenesis, diagnosis, and management. Am J Med 1999;107:262-7.
4. Rubinstein D, McInnes IE and Duddley FJ. Hepatic hydrothorax in the absence of clinical ascites: diagnosis and management. Gastroenterology 1985;88:188-91.
5. Garcia, Nelson Jr, Mihas, Anastasios A. Hepatic Hydrothorax : Pathophysiology, Diagnosis, and Management. Journal Clinical Gastro 2004;38(1)52-8.
6. Camron Kiafar ; Nooman Gilani. Hepatic Hydrothorax : Current concepts of pathophysiology and treatment options. Annals of Hepatology 2008:October-December: 313-20.
7. Alberts WM. Salem AJ, Solomon DA, Boyce G. Hepatic Hydrothorax, cause and management. Arch Intern Med 1991;151:2383-8.
8. Bhattacharya A, Mittal BR, Biswas T, Dhiman RK, Singh B, Jindal SK and Chawla Y. Liver cirrhosis : Bacterial peritonitis, pleural effusion and encephalopathy. Radioisotope scintigraphy in the diagnosis of hepatic hydrothorax. J Gastroenterol Hepatol 2001;16,317-21.
9. Assoouad J, Barathes FP, Shaker W, Soouilamas R and Riquet M. Recurrent pleural effusion complicating liver cirrhosis. Ann Thorac Surg 2003;75:986-98.
10. Lieberman FL, Hidemura R, Peters RL, Reynolds TB. Pathogenesis and treatment of hydrothorax complicating cirrhosis with ascites. Ann Intern Med 1966;64:341-51.
11. Johnston RF, Loo RV. Hepatic hydrothorax. Studies to determine the source of the fluid and report of thirteen cases. Ann Intern Med 1964;61:385-401.
12. Singer, J. A., Kaplan, N. M. & Katz, R. L. Cirrhotic pleural effusion in the absence of ascites. Gastroenterology 1977; 73:575-7.
13. Lazaridis KN, Frank JW, Krowka MJ, Kamath PS. Hepatic Hydrothorax: Pathogenesis, Diagnosis and Management. Ann J Med 1999;107:262-7.
14. Alberts WM, Salem AJ, Solomon DA, et at. (1991). Hepatic hydrothorax. Cause and management. Arch Intern Med 151:2383-8.
15. Light RW-Hepatic hydrothorax. Pleural diseasis 1983; 72-6.
16. Milanez de Campos JR , Filho LOA, de Campos Werebe E, Sette H, Fernandez A, Filomeno LTB, Jatene FB. Thoracoscopy and talc poudrage in the management of hepatic hydrothorax. Chest 2000;118:13-7.
17. Emerson PA, Davies JH. Hydrothorax complicating ascites. Lancet 1955;1:487-8.
18. Mouroux J, Perrin C, Venissac N, Blaive B, Richelme H. Management of pleural effusions of cirrhotic origin. Chest 1996;109:1093-6.
19. Huang PM, Chang YL, Yang CY, Lee YC. The morphology of diaphragmatic defects in hepatic hydrothorax : thoracoscopic finding. J Thorac Cardiovasc Surg 2005; 130:141-5.
20. Cem Aygum, Hakan Demir, Omer Senturk. Differential Diagnosis of Hepatic hydrothorax by ^{99m}Tc Sulfur Colloid Peritoneal Scintigraphy : Two cases. Gasteoenterology Research 2009;2(4):248-52.

THE ASEAN JOURNAL OF RADIOLOGY 2012: 18(3): 151-158 151

Original Article

^{131}I Effective Half-Life in Well Differentiated Thyroid Cancer Patients

Sureerat Saengsuda

Division of Nuclear medicine, Department of Radiology, Rajavithi Hospital, Bangkok, Thailand

Abstract

Background: Oral administration of radioiodine (^{131}I) has been used in treatment of well differentiated thyroid cancer (DTC) after surgery to decrease recurrence and mortality. Patients with high dose ^{131}I administration (>2.96 GBq) requires hospitalization with isolation ward for radiation precautions to limit the radiation dose to family members and members of the public. The advised precautions are generally based on radiation dose rate and effective half-life for clearance of radioactive body burden.

Objective: To assess the effective half-life of ^{131}I in DTC patients who had been administered high-dose ^{131}I (>2.96 GBq).

Material and method: From January 2009 to February 2012, a retrospective review of total 200 DTC patients with age range 8-80 years, mean age 41.98 ± 15.57 years, 173 women and 27 men treated postoperatively with high dose ^{131}I administration were collected for this study. The range of ^{131}I administered activity was 3.18-8.51GBq with the mean activity was 4.82 ± 1.0 GBq. Two measurements of exposure rates at 1 m in μSv/h at initial exposure (E_0) immediately after ^{131}I administration and late exposure at t time (1-3 days later, E_t) were used for calculation of effective half-life of clearance of administered activity.

Result: The range of ^{131}I administered activity was 3.18- 8.51GBq with the mean activity was 4.82 ± 1.0 GBq. The mean initial exposure rates of total patients 81.65 ± 32.36 (E_0) and 17.55 ± 15.94 (E_t) μSv/h were shown with the mean duration time between E_0 and E_t 61.68 ± 24.48 h. The mean effective half-life of ^{131}I clearance was 13.2 ± 12.96 h and the median effective half-life was 9.60 h.

Conclusion: In DTC patients receiving ^{131}I administration after surgery, the value of effective half-life is in accordance with the previous reports in literature. Patient release planning should be differentiated on the basis of individual measurements of exposure rate and calculation of effective half-life.

Radioiodine (^{131}I) is common used in well differentiated thyroid cancer (DTC) patients to ablate thyroid remnants after total or near total thyroidectomy and to treat patients with persistent, recurrent or metastatic cancer. ^{131}I treatment is based on the radiation-induced cell damage caused by the emission of high-energy β-radiation. ^{131}I is a β-emitting radionuclide with a maximum energy of 0.606 MeV and an average energy of 0.192 MeV (range in tissue, 0.8 mm) and has a principal γ-ray of 364 keV with physical half-life 8.06 d. Generally, DTC cells concentrate ^{131}I to a significant degree. These include papillary, follicular and mixed papillary-follicular cancers. Ablation with ^{131}I after initial total or near total thyroidectomy decreases the risk of recurrence and death.[1] The effective half-life in the body is the time required for the amount of a radioactive element deposited in a living organism to be divided by a factor of 2, from the combined action of physical decay and biologic disappearances and not dependent on the administered activity. The effective half-life of ^{131}I links to the effective radiation dose (absorbed dose) to the remnant thyroid tissue and cancer cell which directly link to the effectiveness and efficacy of ^{131}I therapy. Patients with high dose ^{131}I administration have usually been hospitalized to minimize the external radiation dose to family members and the general public. In Thailand, the Society of Nuclear Medicine of Thailand subscribes to the activity limit criteria. DTC patients receive ^{131}I dose >1.1 GBq, or the emitting radiation dose rate at 1 m is >50 μSv/h have to be hospitalized in isolation rooms for 24-72 h. For the general public, the established dose limited is 1 mSv/y, as has been recommended by the International Commission on Radiological Protection (ICRP).[2] The assessment of external radiation exposure from patient to calculate effective half-life instead of physical half-life is a common and necessary practice to evaluate the potential for absorbed dose.

The purpose of this study was to assess the effective half-life of ^{131}I in DTC patients who had been administered high-dose ^{131}I (>2.96 GBq).

Material and Method

Subject

This was a retrospective study of 200 cases from medical records of DTC patients treated with high-dose of ^{131}I who required overnight hospitalization to receive 200 oral doses of ^{131}I in capsule form January 2009 to February 2012. All of them had undergone total or near total thyroidectomy and had thyroid hormone withdrawal 4-5 weeks to obtain a serum TSH level above 30 mU/L on the day of ^{131}I administration to increase NIS (sodium iodide symporter).[3] Blood examinations (TSH, Tg, TgAb, BUN, creatinine) were also done before administration for patient assessment. All patients were given initial ablative doses after surgery or subsequent doses for treatment of both local tumors and distant metastases. The administered activity of ^{131}I ranged from 3.18-8.51 GBq. Each patient was informed about the procedure and gave written consent concerning ^{131}I treatment and radiation protection. Patients were hospitalized for 24-72 h in isolation rooms in the radiotherapy ward until their exposure rates were low enough to meet the discharge criteria. Criterion for discharge was exposure rate below 50 μSv/h at 1 m. Abundant hydration and laxatives were given during hospitalization. The patients who got low-dose or medium dose of ^{131}I (less than 2.96 GBq) were excluded from the study.

Measurement and definition

Two measurements of exposure rates at 1 m from each patient were performed at initial exposure (E_0) measured immediately after ^{131}I ingestion and late exposure at t time (24-72 h later, E_t).[4,5] The exposure rates were performed by using a survey meter, Ludlum model 3. The effective half-life was calculated based on two exposure rates (E_0 and E_t) using the equation below.

$$A_t = E_t * (A_0 / E_0)^{4.6}$$

Where A_t is retained activity at t h (in GBq), A_0 is the administered activity (in GBq), E_t the exposure rate (in μSv) at 1 m from the patient at t h and E_0 is the initial exposure rate (in μSv) at 1 m immediately after ingestion of the ^{131}I capsule.

From the calculation of the retained activity, the effective half-life was calculated using equation below.

$$A_t = A_0 e^{-0.693t/\,Teff}\ 6$$

Where T_{eff} is the effective half-life and t is the elapsed time after ^{131}I administration.

Statistics

Quantitative data were expressed as mean, standard deviation (SD) and median. Qualitative data were shown as percentages. SPSS version 17.0 was used for statistical analysis.

Result

The patients and tumor characteristics were reported in the table 1. For total 200 DTC patients, there were 173 women and 27 men with age range 8-80 years, mean age 41.98 ± 15.57 years. All pathologies of thyroid cancers were papillary type 158 cases (79%), follicular type 36 cases (18%) and mixed type 6 cases (3%). For TNM classification, most common groups were T1+T2 108 cases (54.0%), no lymph node metastases 116 cases (58%), no distant metastases 180 cases. (90%) Most of the patients were in stage I 122 cases (61%) and stage II 30 cases (15%). Figure 1 shows the details of administered activities of ^{131}I in all thyroid cancer patients. The minimum and maximum doses were 3.18 GBq and 8.51 GBq with the mean activity was 4.83 ± 1.1 GBq. The mean administered activity in GBq, mean initial exposure rate (E_0), mean exposure rate at t time (E_t) in μSv/hr, mean duration time between E_0 and E_t in h were demonstrated in table 2. The mean initial and late exposure rates of total patients 81.65 ± 32.36 (E_0) and 17.55 ± 15.94 (E_t) μSv/h were shown. The mean duration time between E_0 and E_t was 60.72 ± 20.88 h. The mean effective half-life of ^{131}I clearance was 13.2±12.96 h.

Discussion

The radiation doses delivered to normal and neoplastic thyroid tissue were often estimated after ^{131}I administration therapeutic in clinical practice.[7-9] Data published in report 53 of the International Commission on Radiological Protection (ICRP)[10] could be used for dose estimates in healthy subjects but these data were irrelevant in thyroid cancer patients for many reasons such as after total or near total thyroidectomy, during hypothyroidism after thyroid hormone withdrawal, decreased renal clearance, different bio-distribution, etc.

There were many methods based on whole body retention, quantitative whole-body scanning, and urinary radioactive measurement to determine residence time for calculation of body burden after ^{131}I therapeutic administration. The present study used exposure rate measurement as a method for

Table 1 Patient and tumor characteristics

		Total (n=200)	
		Number	Percent
Gender			
	Female	173	86.5
	Male	27	13.5
Age (years)			
	Mean ± SD (min-max)	41.98 ± 5.57 (8-80)	
Pathology			
	Papillary	158	79.0
	Follicular	36	18.0
	Mixed	6	3.0
T			
	T1+T2	108	54.0
	T3+T4	45	22.5
	Tx	47	23.5
N			
	N0	116	58.0
	N1	70	35.0
	Nx	14	7.0
M			
	M0	180	90.0
	M1	20	10.0
Stage			
	I	122	61.0
	II	30	15.0
	III	21	10.5
	IV	20	10.0
	Unknown	7	3.5
TSH (mU/L)	Mean ± SD (min-max)	51.53 ± 28.65 (0.7-176.88)	
Tg (ng/ml)	Median (min-max)	13.55 (1-1,152)	
TgAb (IU/ml)	Median (min-max)	12 (1-3,802)	
BUN (mg/ml)	Mean ± SD (min-max)	10.98 ± 4.71 (1-27)	
Creatinin (mg/ml)	Mean ± SD (min-max)	1.06 ± 0.82 (0.5-8.9)	

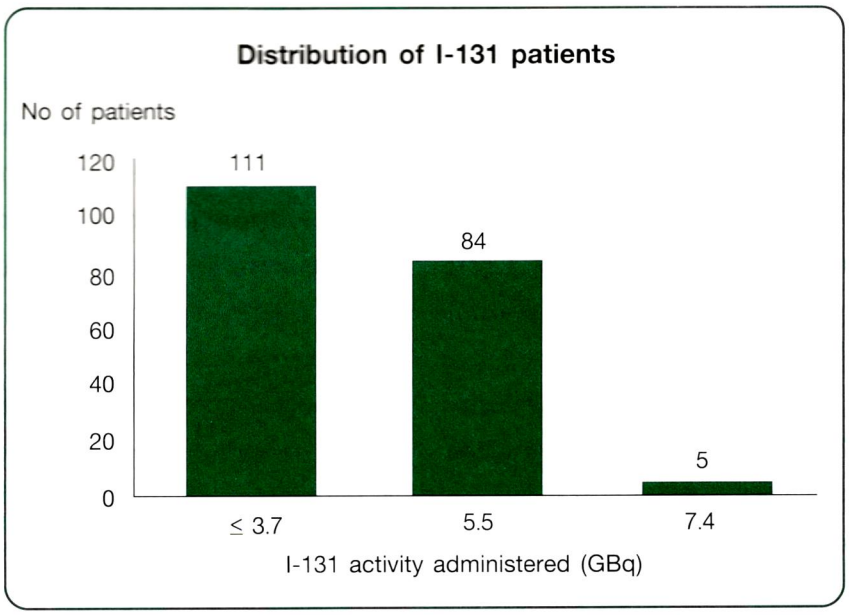

Fig.1 Details of administered activities in DTC patients

Table 2 Mean, SD, median of ^{131}I administer activity, exposure rates, time and effective half-life

	Total (n=200)
^{131}I Administered activity (GBq)	
Mean ± SD	4.83 ± 1.1
Median (Min-Max)	4.02 (3.18-8.51)
Initial exposure rate (E_0, μSv/h)	
Mean ± SD	81.65 ± 32.36
Median (Min-Max)	70 (50-200)
Late exposure rate (E_t, μSv/h)	
Mean ± SD	17.55 ± 15.94
Median (Min-Max)	12 (1-100)
Time between initial and late exposure rate (h)	
Mean ± SD	60.72 ± 20.88
Median (Min-Max)	55.92 (40.32-142.32)
Effective half-life (h)	
Mean ± SD	13.2 ± 12.96
Median (Min-Max)	9.6 (3.84-108)

calculation of ^{131}I body burden which was a daily work for radiation protection in ^{131}I treatment in DTC patients. Thomas SR et al[11] revealed that direct exposure rate measurements showed the potential for being an accurate, reliable and safe method of monitoring patient's ^{131}I body burden. The mean and SD values of ^{131}I dose of total patients was 4.83 ± 1.1 GBq. The mean, SD values of the initial exposure rate (E_0) was 81.65 ± 32.26 μSv/h and late exposure rate (E_t) was 17.55 ± 15.94 μSv/h after average 60.72 ± 20.88 h. In the present study, the exposure rate at 1 m was averaged over measured values and represented along with substantial variations of ranges since there were many variables, such as patient group, administered activity, age, sex, TNM and staging. These values gave an estimate of the risk of radiation levels during patient isolation in the ward. These data were in accordance with the study by Tsuchimochi S et al.[12] They reported the mean and SD values of the exposure rates in patients treated with 3.7 GBq of ^{131}I, the mean and SD values of the exposure rates changed as follow: after 48 h, 20 ± 15; 72 h, 10 ± 9 μSv/h respectively. The present study revealed the exposure rates 17.55 ± 15.94 μSv/h at 61.68 ± 24.48 h (E_t) which was in range between 48 and 72 h as reported by Tsuchimochi S et al.

Ravichandran R, et al[13] used the mean measured exposure rate at 1 m in μSv/h immediately after ^{131}I administration and at 24 h intervals for estimation of effective half time of ^{131}I clearance of administered activity. The mean and SD values of administered activity of ^{131}I in treatment of thyroid cancer patients was 4.36 ± 1.17 GBq (n=69) which was in accordance with this study (4.82 ± 1.07 GBq). Their measured exposure rates in μSv/h from patients post ^{131}I administration were 88 ± 37.6 at 0 h, 30.1 ± 21.6 at 24 h, 11.6 ± 7.4 at 48 h, 6.3 ± 6.4 at 72 h, 4.12 ± 4.6 at 96 h. This study showed the exposure rate 81.65 ± 32.26 μSv/h immediately after ^{131}I ingestion (E_0) which was in correspondence. However, there was much decreased exposure rate at 48 and 72 h reported by R Ravichandran et al[13] as compared with the present study probably due to different tumor and patient characteristics.

The thyroid tissues of DTC patients were removed by total or near total thyroidectomy and/or ablated by prior doses of ^{131}I before treatment of larger dose of ^{131}I. These made ^{131}I retaining in the body compartments be relatively small and the effective half-life of ^{131}I, combining physical and biological eliminations, was quite short.[14] The U.S. Nuclear Regulatory Commission (NRC) published a guidance document[15] includes an example for ^{131}I, which assumed effective half-life of 7.7 h for the extra thyroidal component of the retained activity and also assumed that this component was about 95% of the total. In this study, the mean effective half-life was 13.2 ± 12.96 h. Thus, the value of 7.7 h for the extra thyroidal ^{131}I by NRC was less than the mean effective half-life from this study approximately a factor of two. However, the mean effective half-life in this study was in agreement with previous reported values 11.2-15.4 h[13,16] in Indian population and the values reported by Barrington SF et al[17] 9.4 h, 13.4 h and 12 h for measurements at 0.1 m, 0.5 m and 1.0 m respectively. The results reported by other investigators[11,18,19] also indicated that ^{131}I clearance in DTC patients after surgery had a faster component in the range of within 12 h. From previous published studies, there were wide variations in the values of effective half-life reported by other investigators.[20,21] Remy H et al[23] reported the mean effective half-life 15.7 ± 5.3 h in 218 DTC patients

who underwent surgery and thyroid hormone withdrawal follow by ^{131}I administration of 1.11-3.7 GBq. David L et al reported a median effective half-life of at least 14 h and mean effective half-life of 17.1 h of 250 administrations of ^{131}I for thyroid cancer with substantial variations and proposed that discharge criteria for radiation safety purposes should be calculated on the basis of individual measurements.

For radiation protection and precautions of radiation hazards to limit the radiation dose to nursing staff during patient stay in wards, patients were routinely admitted in hospital 48-72 h after ^{131}I administration in isolation ward. For faster clearance of ^{131}I in DTC patients after surgery, patients could be released earlier before 48 h. The exposure rates at 24, 48 and 60 h should be monitored for every patient in order to possible earlier discharge with radiation safety. Releasing patients earlier from isolation ward had several advantages: lower health care cost, lower doses to nursing staff, and psychological benefits for patients and families.[23] For further modifications, ^{131}I treatment could be administered at home or outpatient setting even patients receiving high dose ^{131}I administration due to short effective-half life of ^{131}I clearance. However, selected patients, family members and suitable domestic circumstances should be also considered for outpatient setting in individual cases.

Conclusion

Exposure rate measurement is one of effective method of assessing the patient body burden following ^{131}I treatment. It is accurate, reliable and relatively safe method of monitoring the patient body burden. The value of effective half-life is in accordance with the previous reports in literatures. For practices in radiation protection to keep doses to nursing staffs and other members "as low as reasonably achievable", patient release planning should be differentiated on the basis of individual measurements of exposure rate and calculation of effective half-life.

Study Limitation

The principle source of error in exposure rate measurement was probably inaccuracy in the distances to the central body axis of each patient. Variations due to measurements by different technologists were also noticed.

References

1. Varma VM, Beirwaltes WH, Nofal MM, Nishiyama RH, Copp JE. Treatment of thyroid cancer death rates after surgery and after surgery followed by sodium iodide-131. JAMA 1970;214:1437-42.
2. International Commission on Radiological Protection. Recommendations of the International Commission on Radiological Protection. New York, NY: pergamon Press; 1991. ICRP publication 60.
3. Luster M, Clarke SE, Dietlein M, Lassmann M, Lind P, Oyen WJ, et al. Guidelines for radioiodine therapy of differentiated thyroid cancer. Eur J Nucl Med Mol Imaging 2008;35:1941-59.
4. Thompson MA. Radiation safety precautions in the management of the hospitalized (131) I therapy. J Nucl Med Technol 2001;29:61-6.
5. Matovic MD, Jankovic SM, Jeremic M, Tasic Z, Vlajkovic M. Unexpected effect of furosemide on radioiodine urinary excretion in patients with differentiated thyroid carcinomas treated with iodine 131. Thyroid 2009;19: 843-8.
6. Papadimitriou D, Kottou S, Oros L, Ilias I, Molfetas M, Tsapaki V, et al. Differentiated thyroid cancer: comparison of therapeutic iodine 131 biological elimination after discontinuation of levothyroxine versus administration of recombinant human thyrotropin 2006;20:63-67.
7. Hanscheid H, Lassmann M, Luster M, Thomas SR, Pacini F, Ceccarelli C, et al. Iodine biokinetics and dosimetry in

radioiodine therapy of thyroid cancer: procedures and results of a prospective international controlled study of ablation after rhTSH or hormone withdrawal. J Nucl Med 2006;47:648-54.

8. Maxon HR III, Smith HS. Radioiodine-131 in the diagnosis and treatment of metastatic well differentiated thyroid cancer. Endocrinol Metab Clin North Am 1990;19: 685-718.
9. Schlumberger M, Lacroix L, Russo D, Filetti S, Bidart JM. Defects in iodine metabolism in thyroid cancer and implications for the follow-up and treatment of patients. Nat Clin Pract Endocrinol Metab 2007;3:260-9.
10. ICRP. Radiation Dose to Patients from Radiopharmaceuticals. Vol 18. Oxford, UK.: Pergamon Press; 1987:ICRP publication 53.
11. Thomas SR, Maxon HR, Fritz KM, Kereiakes JG, Connell WD. A comparison of methods for assessing patient body burden following 131-I therapy for thyroid cancer. Radiology. 1980;137:839-42.
12. Tsuchimochi S, Nakajo M, Umanodan T, Fokoshima N, Shigaki S, Kiku T. A study on the isolation period of patients with metastatic thyroid cancer treated by ^{131}I according to a new guideline 2001;38:747-54.
13. Ravichandran R, Binukumar JP, Saadi AA. Estimation of effective half life of clearance of radioactive Iodine (^{131}I) in patients treated for hyperthyroidism and carcinoma thyroid. Indian J Nucl Med 2010;25:49-52.
14. North D, Shearer D, Hennessey J, Donovan G. Effective half-life of ^{131}I in thyroid cancer patients. Health Phys 2001;81:325-9.
15. US Nuclear Regulatory Commission. Release of patients administered radioactive materials. Washington, DC: US Government Printing Office; 1997:Regulatory guide 8.39.
16. Ravichandran R, Supe SS, Jayasree U, Devaru S. Measurement of the radioactive body burden in patients receiving Iodine-131 treatments for carcinoma of the thyroid. Euro J Nucl Med 1997;24(4):464.
17. Barrington SF, Kettle AG, O'Doherty MJ, Wells CP, Somer EJ, Coakley AJ. Radiation dose rates from patients receiving Iodine-131 therapy for carcinoma thyroid. Euro J Nucl Med 1996;23:123-30.
18. Castronovo FP Jr, Bep RA, Veilleux NM. Dosimetric considerations while attending hospitalized I-131 therapy patients. J Nucl Med Tech 1983;10:157-60.
19. Culver CM, Dworkin HJ, Radiation safety considerations for post-iodine-131 hyperthyroid therapy. J Nucl Med 1991;32:169-73.
20. Menzel C, Kranert WT, Dobert N, Diehl M, Fietz T, Hamscho N, et al. rhTSH stimulation before radioiodine therapy in thyroid cancer reduces the effective half-life of ^{131}I. J Nucl Med 2003;44:1065-8.
21. Travis CC, Stabin MG. ^{131}I ablation treatment in young females after the Chernobyl accident. J Nucl Med 2006; 47:1723-7.
22. Remy H, Borget I, Leboulleux S, Guilabert N, Lavielle F, Garsi J, et al. ^{131}I Effective Half-Life and Dosimetry in Thyroid Cancer Patients. J Nucl Med 2008;49:1445-50.
23. Venencia CD, Germanier AG, Bustos SR, Giovannini AA, Wyse EP. Hospital Discharge of Patients with Thyroid Carcinoma Treated with ^{131}I. J Nucl Med 2002;43:61-5.

THE ASEAN JOURNAL OF RADIOLOGY 2012: 18(3): 159-166 159

Original Article

The Accuracy of Transthoracic Sonography in Detection of Pneumothorax

Orawan Autravisittikul, MD., Lukana Jirapong, MD., Pariyanoot Deesuwan, MD.

Department of radiology, Samutsakhon Hospital, Samutsakhon

Abstract

Objective: To evaluate the accuracy of transthoracic sonography in detection of pneumothorax

Materials and methods: The prospective study of 48 patients who were sent to chest radiograph at the radiologic department for excluded pneumothorax and then transthoracic ultrasound was performed with blindly result of chest radiograph. The sonographic sign of pneumothorax includes absent lung sliding, loss of comet tail artifact, lung point and stratosphere sign were evaluated and the results of pneumothorax between two modalities were compared. If discrepancy between transthoracic sonography and chest radiograph was found then further CT scan was performed either CT scan or ICD was confirmed in all case of pneumothorax. The accuracy of the transthoracic sonography and the chest radiograph in detection of pneumothorax were compared.

Results: There were 6 patients positive pneumothorax by transthoracic sonography and 5 patients positive pneumothorax by chest radiograph. There were 7 of 48 patients (14.58%) confirmed positive for pneumothorax by CT or chest tube placement with air rush from the tube drain. The 5 of 7 patients of positive pneumothorax were ICD placement and 2 patients were conservative treatment. The accuracy of transthoracic sonography and chest radiograph is 93.7 and 91.6 respectively. The sensitivities, specificities, negative predictive values (NPVs) and positive predictive values (PPVs) for detection pneumothorax of transthoracic U/S is 71.4%, 97.6%, 95.2% 83.3% and of chest radiograph is 57.1%, 97.6%, 93%, 80% respectively.

Conclusion: High accuracy of transthoracic sonography and high sensitivity of transthoracic sonography compared with the chest radiograph in detection of pneumothorax. Transthoracic U/S should be an alternative primary survey or in Extended FAST to get more information and helpful to detection of pneumothorax and prompt treatment to the patient.

Keywords: Pneumothorax, Transthoracic sonography, Accuracy

Introduction

The first reported use of ultrasound to detect pneumothorax in human was by Wernecke K. et al since 1987[1]. However there is slow acceptance due to the traditional teaching that air filled lungs are not ultrasound friendly: The chest radiograph is the primary modality in detect pneumothorax but the sensitivity has been reported vary range from 25-75%[2]. Although the Computed tomography (CT) is the gold standard for the detection of pneumothorax, it is neither practical nor feasible to perform this imaging examination in all patients to rule out pneumothorax[2,3]. Transthoracic sonography is another quick modality to rule in and rule out for pneumothorax, able to perform at bedside and has no risk associated with repeated measures[4]. There is gradually rapid evolving and many researches about this investigation for the past decade. However in our institute; the transthoracic sonography to exclude pneumothorax was not well established. The aim of this study is to prospectively compare the accuracy of transthoracic US with that of chest radiography in the detection of pneumothorax in our institute.

Material and Method

The prospective study of patients who were sent to chest radiograph at the radiologic department for excluded pneumothorax including blunt chest injury with chest pain, stab wound at chest, patient with multiple trauma or patient sent to ultrasonography in traumatic patient (Extended FAST) from June 2012 to Dec 2012. The study protocol was approved by the ethical committee of the hospital. The informed consent was waived due to traumatic emergency patient and contemporaneous collection of data did not require to follow up identifying information. The exclusion criteria includes unstable patient as follow : 1. Glasglow coma score below eight 2. severe chest wall injury including extensive subcutaneous emphysema 3. shock 4. post cardiac arrest. The patient was chest radiographed and then transthoracic ultrasound was performed by radiologist with blindly result of chest radiograph. The sonography was performed after chest radiograph within 30 minutes using 3.5-5 MHz curvilinear and 5-10 MHz Linear probe (Logiq 7 and S8; GE healthcare). The sonography was performed at anterior and lateral chest wall along upper, middle and lower at mid clavicular line and mid axillary line by using firstly convex probe with decreased depth for screening and then linear probe for fine detail of pleural line.

There are sonographic signs of transthoracic sonography in normal aerated lung[5]. First "lung sliding" : there should visualize the hyperechoic pleural line in between two ribs with to-and-fro movement of the visceral pleura on parietal pleura in normal aerated lung (Fig 1a). In M-Mode with cursor place over the pleural line and there are two different pattern on screen : the motionless of the chest above the pleural line creates horizontal wave and the sliding below the pleural lines creates a granular pattern seen as waves crashing in onto the sand "seashore sign" (Fig 1b). Second "comet-tail artifact" are reverberation artifacts appear as hyperechoic vertical line that extend from the pleura to the edge of screen and moving synchronously with lung sliding and respiratory movement (Fig 1a). The present of lung sliding and comet tail artifact at the pleural interface indicates apposition of the pleural surface without pneumothorax. In pneumothorax ; there is air in pleural cavity prevents visualized visceral pleura resulting "absent lung sliding" in B-mode and "stratosphere sign" in M-mode. There is

also another sonographic sign includes "lung point" showing sonographic sign between the pneumothorax and the aerated lung[5,12]. The sonographic criteria for diagnosis pneumothorax includes absent lung sliding, loss of comet tail artifact, lung point and stratosphere sign in M-mode.

The chest radiograph was evaluated after sonography. The chest radiograph and sonography were evaluated by radiologist which could have been either by the same or a different radiologist according to availability.

Concordance of pneumothorax between the transthoracic sonography and chest radiograph was considered to be sufficient for diagnosis or exclusion of pneumothorax[6]. If positive concordance for pneumothorax ; the diagnosis was confirmed by either CT scan or air released from the chest tube. If negative concordance for pneumothorax; no further investigation was needed except clinical presentation was very suspicious or to evaluate other causes; then further CT was performed. If discrepancy between transthoracic sonography and chest radiograph was found then further CT was performed.

The specificity, sensitivity, positive predictive value (PPV), negative predictive value (NPV) and accuracy of transthoracic sonography and chest radiograph were calculated.

Results

The total 49 patient was screening to transthoracic sonography and one patient was excluded due to extensive subcutaneous emphysema and unable to evaluate the underlying lung parenchyma. The 48 patients were included in this study (36 male, 12 female; mean age 42 years SD= 17.43 years, age range 11-80 years). There were 7 of 48 patients (14.58%) confirmed positive for pneumothorax by CT or chest tube placement with air rush from the tube drain. The 5 of 7 patients of positive pneumothorax were ICD placement and 2 patients were conservative treatment. The results of the study are as Table 1

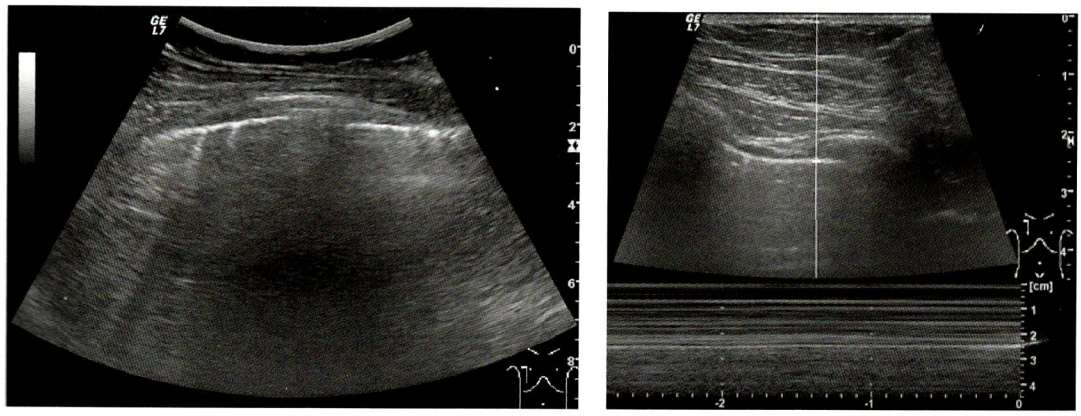

a. b.

Fig. 1 **Normal lung** a. in B-mode : Transthoracic sohography revealed hyperechoic pleural line in between two ribs and to-and-fro movement of the visceral pleura on parietal pleura in normal aerated lung "lung sliding" during real time study and "comet tail artifact" synchronized with respiratory movement. b. in M-mode : The motionless portion of the chest above the pleural line creates horizontal wave and the sliding below the pleural lines creates a granular pattern seen as waves crashing in onto the sand "seashore sign"

In the five positive concordance pneumothorax by both transthoracic sonography and chest radiograph were confirmed positive pneumothorax by CT and ICD placement in four patients. There was one patient that CT showed a large subpleural bullae with fibrosis at left apex with no pneumothorax (false positive US and chest radiograph) (Fig 2). In this case transthoracic sonography showed localized pleural thickening at left apex but absent lung sliding and comet tail artifact and CXR showed fibrosis with parenchymal distortion at LUL and questionable localized pneumothorax at left apex.

Table 1 The results of the transthoracic sonography and chest radiography for pneumothorax

Finding Pneumothorax	Transthoracic sonography	Chest radiograph	Number of patients	Number of diagnosis Pneumothorax
Positive concordance	+	+	5	4
Discordance	+	-	1	1
Negative concordance	-	-	42	2

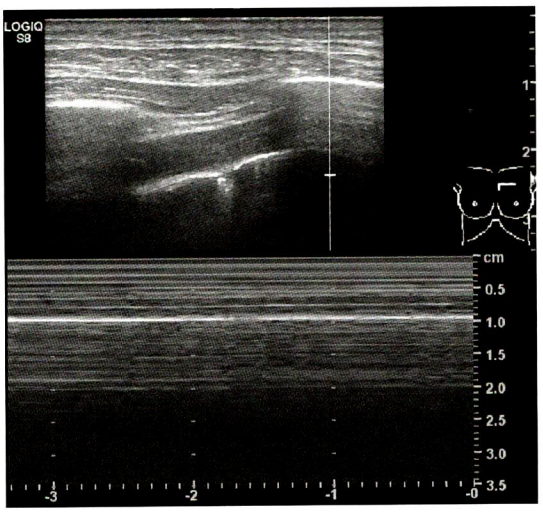

a.

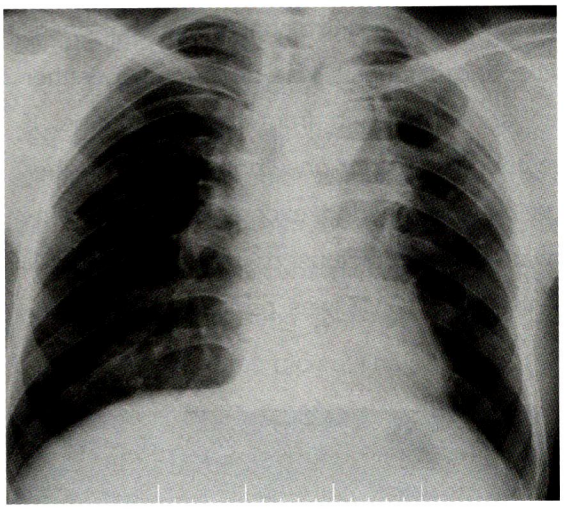

b.

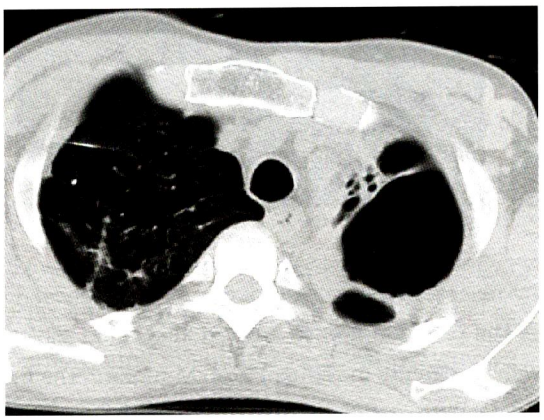

c.

Fig.2 **False positive pneumothorax** a. U/S reveals absent lung sliding and comet tail artifact and provisional diagnosis of pneumothorax. b. CXR showed fibrosis with parenchymal distortion at LUL and questionable localized pneumothorax at left apex. c. CT showed a large subpleural bullae with fibrosis at left apex with no pneumothorax. In this case; there is focal pleural thickening and disruption of the pleural line on transthoracic sonography; old inflammatory pleura with subpleural bleb/bullae should be awareness.

In the one discordance finding which sonography revealed positive for pneumothorax discrepancy with chest radiograph and CT scan was confirmed positive pneumothorax and ICD placement after diagnosis (Fig 3).

In the 42 negative concordance pneumothorax ; there were two patients sending to CT scan; one patient was sent to exclude intra-abdominal injury and the other was multiple fracture ribs with severe chest pain to rule out intrathoracic injury. The first one showed localized pneumothorax subjacent stab wound at left posterior lower chest and the other one showed minimal medial pneumothorax. Both patients had conservative treatment without ICD placement.

There was none of patient with negative transthoracic sonography but positive chest radiograph for pneumothorax in this study.

The sensitivities, specificities, negative predictive values (NPVs) and positive predictive values (PPVs) of the transthoracic sonography and chest radiograph are shown on table 2.

Other finding during U/S demonstrated sternal fracture in one patient and additional lateral radiograph confirmed the diagnosis. The other case showed fracture right lateral rib at the point of tenderness during sonography and CXR showed the corresponding fracture.

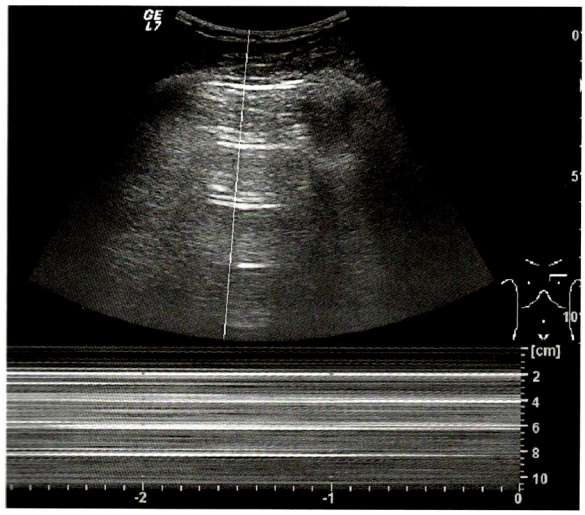

a.

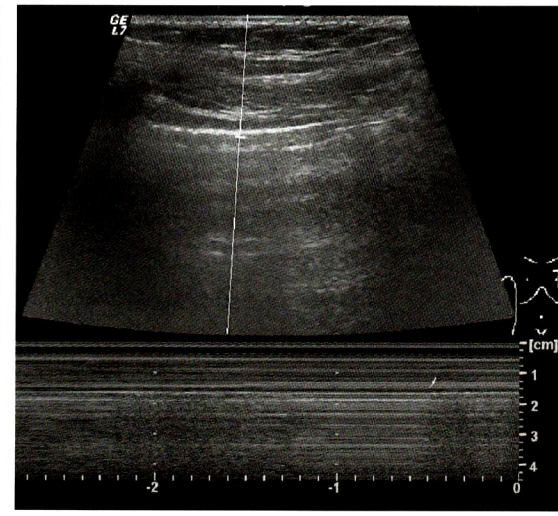

b.

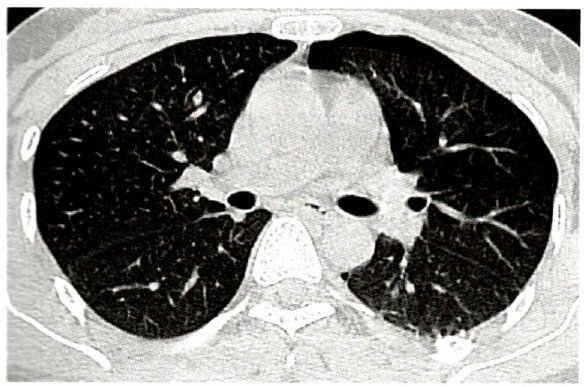

c.

Fig.3 Pneumothorax a. Transthoracic sonography revealed absent lung sliding and also present of ring down artifact and M-mode reveals "stratosphere sign" b. "lung point" showing sonographic sign between the pneumothorax and the normal aerated lung in M mode (from normal lung to pneumothorax and then back again). c. CT scan confirmed pneumothorax at left anterior chest

Table 2 The parameter of compared between transcthoracic sonography and chest radiograph

Parameters	Transthoracic sonography (US) %	Chest radiograph (CXR)%
Sensitivity	71.4	57.1
Specificity	97.6	97.6
Negative predictive value (NPVs)	95.2	93
Positive predictive value (PPVs)	83.3	80
Accuracy	93.7	91.6
Likelyhood ratio	29.75	23.79
P-value	<0.001	<0.001

Discussion

Chest radiograph is the primary diagnostic modality used to screen for pneumothorax but the sensitivity is slightly low range from 25% to 75%[2]. CT is the most sensitive method and gold standard for diagnosing pneumothorax, but it cannot be considered as the method of choice in all clinical practice cases because of the high ionizing radiation exposure, the cost and sometimes the difficulty in transporting patient; particularly in severe traumatic patient and critically ill patient in intensive care unit[6,16]. The transthoracic ultrasound could be the alterative or complementary modality to detect the pneumothorax. The use of sonography for diagnosis of pneumothorax was established for more than twenty years but the clinical applied usage was not well known by clinician.

In the review literature ; the overall sensitivity of transthoracic ultrasonography for the diagnosis of pneumothorax ranged from 58.9% to 100%, and the specificity ranged from 94% to 100%[6-9,14]. In this study ; the transthoracic sonography was 71.4% sensitivity higher than the chest radiograph (57.1%) (table 2). Both modalities show equal high specificity (97.6%). There was no significant different to the review literature. There is statistically significant that transthoracic sonography and the chest radiograph in the diagnosis of pneumothorax ($p < 0.001$). Transthoracic sonography has been reported to have high negative predictive value in detection of pneumothorax and slightly lower positive predictive value[2,6] which similar results to this study that NPVs and PPVs are 95.2% and 88.3% respectively.

There was one case that chest radiograph did not depict pneumothorax but shown by U/S ; which was confirmed by CT reveals pneumothorax and ICD placement later. After retrospective review of the CXR; it was unable to demonstrate the visceral pleural line seen only deep sulcus at medial costrophrenic angle. This should be the advantage of sonography over the chest radiograph particularly in situation that no CT is available.

There were two false negative cases in both US and CXR but detection on CT scan with small amount of medial pneumothorax and the other showed localized posterior pneumothorax subjacent the stab wound. Both patients were conservative treatment and no ICD needed. This is suggestive of both modalities could be missed the minute pneumothorax which is no clinical significant.

There was one false positive case in both US and CXR due to large subpleural bullue with pleural

thickening /adhesion mimicking localized pneumothorax. Lichtensteun et al. has mentioned that abolition of lung sliding may seen on case atelectasis, pleural symphysis, fibrosis or loss of lung compliance[10]. The bullous emphysema, pachy pleuritis with pleural adhesion, phrenic nerve paralysis with impaired lung excursion are also prevented the visualization of lung sliding simulating presence of pneumothorax. In our observation; if there is associated parietal pleural thickening with non-visualized lung sliding on transthoracic sonography should be aware of false positive due to adhesion / post inflammatory fibrosis. The other sign such as lung point or A line sign (a hyperechoic horizontal artifact arising from the pleural line) are warranted and help to interpretation[10].

In the technical aspect: The lung sliding is easily to detect compared with the comet tail artifact. The sliding amplitude is greater at base than at the apex. At apex it may be imperceptible, but it slightest movement is significant (all-or-nothing rule)[10]. The M-mode and the power doppler also help to detect the excursion and movement of the lung[4,8]. In the experience of this study; the convex probe with adjusting the depth/focus at more superficial location was adequate to evaluate the sonographic sign of pneumothorax. This could apply at the emergency room which is used of convex probe without changing to other probe in trauma examination (Extended FAST). Soldati G. et al. reported the high diagnostic accuracy of transthoracic sonography even use of convex probe at emergency department[13-14]. The transthoracic sonography could be performed either in the emergency department or in the ICU with mechanically ventilated patients and pneumothorax risk which the early detection of radio-occult pneumothorax can be prevented serious complications. In addition ; the U/S not only helps to diagnose pneumothorax but it allows approximation of pneumothorax size and location of ICD placement as a leading procedure for ICD placement as lung point present[5,11,14]. The limitation of sonography is operator dependent which require some experience to perform but we think that it is not too difficult to perform after short period of training.

In this study ; there was one case of sternal fracture seen during U/S and not seen on routine AP/PA view. In this case; the patient was additional lateral chest radiograph and confirmed the diagnosis of sternal fracture. There was previous report of sonography to detect bone fracture[15]. This could be the advantage of sonography over conventional radiograph which able to direct evaluate the point of the pain and tenderness.

The limitation of this study is smaller number of patient. In this study; not all CT scan in the concordance negative patients were performed due to the cost and also a risk of high radiation exposure. Consequently, it is possible that both transthoracic sonography and chest radiograph were not detected some small pneumothorax but no clinical significant for the patient condition.

Conclusion

The study demonstrates the high accuracy of tranthoracic sonography in detection of pneumothorax and high sensitivity of transthoracic sonography compared with the chest radiograph in detection of pneumothorax. There is false negative in some case of small pneumothorax but no clinically significant. In addition, it should be aware in some case of bullous emphysema or pleural adhesion which can limit excursion of pleura mimic pneumothorax. We would like to encourage the radiologist and also the

clinician whom involves to emergency department to perform additional transthoracic U/S in traumatic patient as bedside primary survey or Extended FAST to get more information and helpful to diagnosis with prompt treatment to the patient.

Acknowledgement

The authors would like to thanks all the related radiologic technologist for assisting in the implementation of this study and Mrs. Nattawan Sangurai for the statistical analysis

References

1. Wernecke K, Galanski M, Peters PE, et al. Pnemothorax : evaluation by ultrasound, preliminary results. J Thorac Imag 1987;2:76-8.
2. Rowan KR, Kirkpatrick AW, Liu D, Forkheim KE, Mayo JR, Nicolau S. Traumatic pneumothorax detection with thoracic US: correlation with chest radiography and CT-initial experience. Radiology 2002;225:210-4.
3. Wall SD, Federle MP, Jeffrey RB, Brett CM. CT diagnosis of unsuspected pneumothorax after blunt abdominal trauma. AJR Am J Roentgenol 1983;141:919-21.
4. Noble VE, Think ultrasound when evaluating for pneumothorax. J Ultrasound Med 2012 Mar;31(3):501-4.
5. Husain LF, Hagopian L, Wayman D, Baker WE, Carmody KA. Sonographic diagnosis of pneumothorax. J Emerg Trauma Shock 2012;5:76-81.
6. Sartori S, Tombesi P, Trevisani L, Nielsen I, Tassinari D, Abbasciano V. Accuracy of transthoracic sonography in detection of pneumothorax after sonographically guided lung biopsy: prospective comparison with chest radiography. AJR Am J Roentgenol 2007 Jan;188(1):37-41.
7. Chung MJ, Goo JM, Im JG, Cho JM, Cho SB, Kim SJ: Value of high-resolution ultrasound in detecting a pneumothorax. Eur Radiol 2005;15:930-5.
8. Blaivas M, Lyon M, Duggal S. A prospective comparison of supine chest radiography and bedside ultrasound for the diagnosis of traumatic pneumothorax. Acad Emerg Med 2005;12:844-9.
9. Alsalim W, Lewis D. Towards evidence based emergency medicine: Best BETs from the Manchester Royal Infirmary. BET 1: Is ultrasound or chest x ray best for the diagnosis of pneumothorax in the emergency department?. Emerg Med J. Jun 2009;26(6):434-5.
10. Lichtenstein DA, Meziere G, Lascols N, Biderman P, Courret JP, Gepner A, Goldstein I, Tenoudji-Cohen M: Ultrasound diagnosis of occult pneumothorax. Crit Care Med 2005;33:1231-8.
11. Chan, S. S. W. (2003), Emergency Bedside Ultrasound to Detect Pneumothorax. Academic Emergency Medicine, 10:91-4.
12. Lichtenstein D, Meziere G, Biderman P, Gepner A. The "lung point": an ultrasound sign specific to pneumothorax. Intensive Care Med 2000;26:1434-40.
13. Soldati G, Testa A, Sher S, Pignataro G, La Sala M, Silveri NG. Occult traumatic pneumothorax: Diagnostic accuracy of lung ultrasonography in the emergency department. Chest 2008;133:204-11.
14. Zhang M, Liu ZH, Yang JX, Gan JX, Xu SW, You XD, etal. Rapid detection of pneumothorax by ultrasonography in patients with multiple trauma. Crit Care 2006;10:R112.
15. Jin W, Yang DM, Kim HC, Ryu KN. Diagnostic values of sonography for assessment of sternal fractures compared with conventional radiography and bone scans. J Ultrasound Med 2006;25(10):1263-8; quiz 9-70.
16. Lichtenstein DA, Menu Y. A bedside ultrasound sign ruling out pneumothorax in the critically ill. Lung sliding. Chest 1995;108:1345-8.
17. Dulchavsky SA, Schwarz KL, Kirkpatrick AW, et al. Prospective evaluation of thoracic ultrasound in the detection of pneumothorax. J Trauma 2001;50:383-8. 2001.

THE ASEAN JOURNAL OF RADIOLOGY 2012: 18(3): 167-183 167

Original Article

Efficacy of Gadoxetic Acid (Gd-EOB-DTPA)-Enhanced MRI in Detecting and Characterizing Focal Liver Lesions

Siriporn Nitjaphanich, MD., Chamaree Chuapetcharasopon, MD

Department of Radiology, Bumrungrad International Hospital, Bangkok, Thailand

Abstract

Objective: To characterize the imaging findings of liver masses among patients who underwent Gd-EOB-DTPA (Primovist®)-enhanced magnetic resonance imaging (MRI) examinations at Bumrungrad International Hospital, Bangkok, Thailand.

Methods: This retrospective case series reviewed and assessed patients' medical records from the computerized Bumrungrad "Hospital 2000" system. MRI scans were conducted before and during arterial and portal venous phases, and in the hepatocyte-selective phase, 10 and 20 minutes after injection of Primovist® for enhanced MRI study. The enhancement patterns and morphologic features of the arterial and portal venous phases, and the hepatocyte-selective phase (at 20 minutes p.i) were evaluated.

Results: Among the 19 cases, there were 21 lesions, consisting of 10 cirrhotic, 11 non-cirrhotic, and 2 known primary cancers. There were 9 benign lesions (42.9%) comprising 2 hemangiomas, 1 venous malformation, 1 nodular reactive hyperplasia, and 5 fibronodular hyperplasia (FNH)/hepatocellular adenomas. Twelve lesions (57.1%) were malignant, comprising 10 hepatocellular carcinomas (HCC) and 2 liver metastases. Only 4 lesions had been confirmed by target-guided biopsies (1 regenerating nodule, 2 HCC, and 1 benign FNH or hepatic adenoma). The remainder were identified conclusively by clinical history after 1-3 years' follow-up. None of 5-FNH had low signal intensity, and had non-hepatocyte uptake in the hepatocyte selective/hepatobiliary (HB) phase. Most HCC cases (90.0%) presented with cirrhosis, and exhibited low signal intensity in the hepatobiliary phase, indicating non-hepatocyte uptake and the absence of any hepatocyte component. However, there were HCC with hepatocyte uptake, indicating the presence of hepatocyte cell components in 20% of the cases in this study. All liver metastases had non-hepatocyte uptake. No acute-contrast observation revealed an adverse reaction in this study.

Conclusion: It has been suggested that gadoxetic/Gd-EOB-DTPA-enhanced MRI studies enable good characterization of liver nodules, using an evaluation of the presence or absence of hepatocyte-cell components, particularly in FNH and/or hepatic adenoma, in contrast with HCC and liver metastases. No adverse reaction was observed after injection with the Gd-EOB-DTPA.

Keywords: Gadoxetic acid (Gd-EOB-DTPA), liver masses, magnetic resonance imaging

Introduction

Magnetic resonance imaging (MRI) is one of the most important modalities for detecting and characterizing liver masses. Multiple-pulse sequences are used to differentiate tissues based on their unique longitudinal relaxation time (T1) and transverse relaxation time (T2). Despite excellent tissue differentiation, a contrast agent is needed to determine the vascular patterns of liver masses. Currently, many magnetic resonance (MR) contrast agents are available to improve lesion detection, and the characterization of liver masses. Contrast-enhanced MRI is generally preferred to non-enhanced MRI and contrast-enhanced computed tomography (CT) in the detection and characterization of liver lesions.[1-8]

Primovist®, (Bayer HealthCare, Leverkusen, Germany) is gadolinium-ethoxybenzyl-diethylene-triamine penta-acetic acid (Gd-EOB-DTPA, gadoxetic acid), a newly developed MR contrast agent. It offers two properties in one injection. The first property is to evaluate tumor vascularity after a bolus injection of Gd-EOB-DTPA, in a manner similar to evaluation with conventional gadolinium triamine penta-acetic acid (Gd-DTPA).[9] The second property is to determine the uptake of functioning hepatocytes. This contrast agent accumulates in normally functioning hepatocytes in the delayed phase (hepatobiliary phase) which begins 20 minutes after injection and lasts until 40 minutes after injection.[9-12] With this combined properties, this contrast agent is very unique for the study of liver masses. Primovist® is among eight gadolinium based contrast agents for MRI licensed by the Thai Food and Drug Administration.[13] Since its introduction at Bumrungrad International (BI) in December 2006, about 20 patients have been administered this agent. Although Primovist® has been tested elsewhere; its safety and efficacy have not yet been documented in Thailand.

Pre-malignant dysplastic nodules or early hepatocellular carcinomas are difficult to diagnose in the background of the cirrhotic liver. Standard MRI with intravenous extracellular agent (Gd-chelate) is a useful technique to detect these lesions, but its sensitivity is still relatively low.[12,14-17] Previous studies have demonstrated the usefulness of the new hepatobiliary contrast agent (Gd-EOB-DTPA) in the detection of liver lesions, particularly in patients with cirrhosis.[7-9,12,18-20] This preliminary study retrospectively documents the imaging findings and detection efficacy of Gd-EOB-DTPA (Primovist®)-enhanced MRI among patients with liver masses whose MRI were performed using Primovist® at Bumrungrad International Hospital. Preliminary safety profiles and adverse events are also described.

Materials and Methods

Setting

The medical records of patients investigated by MRI with intravenous Gd-EOB-DTPA (Primovist®), between December 2006-October 2007, were retrieved from the Hospital's computerized Hospital 2000 Health Information System (currently, Microsoft Amalga Health Information System version 6.0 SP3 http://www.microsoft.com/amalga/default.mspx). With the formal approval of Bumrungrad International Institutional Review Board (IRB) and the Hospital administration, the principal investigator (PI) accessed the relevant medical records. Patient data were linked to the study file via anonymous study identification numbers (IDs), accessible only to the PI. All of the medical records of patients meeting the following inclusion criteria were used in this study.

Inclusion and exclusion criteria

All medical records of patients with liver nodule/nodules ≥1.5 cm in diameter were included. The liver nodules were categorized into three groups, based on the underlying disease--liver nodules due to cirrhosis, metastatic liver nodules due to any primary neoplasm, and benign liver nodules. The final liver-nodule diagnosis was made by histopathology, typical imaging appearance, follow-up investigation, or the results of interventional angiography.

Hepatocellular carcinomas (HCC) could be diagnosed by typical MRI findings: rapid arterial enhancement, and rapid venous or delayed washout, combined with serum alpha-fetoprotein (AFP) >400 ng/mL. Metastatic liver nodules could be diagnosed by history of known primary cancers, rapid growth of liver nodules during MRI or MDCT follow-up studies, combined with high serum carcinoembryonic antigen (CEA). There were no exclusion criteria.

MRI protocol:

Radiologic studies were performed by two high-field MRI machines, using either 1.5 Tesla General Electric EXCITE II (GE Healthcare, Chalfont St Giles, Bucks, UK) or 1.5 Tesla MAGNETOM Avanto (Siemens Medical Solutions USA, Inc., Malvern, PA, USA). Non-contrast MRI pulse sequences consisted of axial T1-weighted (T1W) spin echo (SE), T2-weighted (T2W) spin echo (SE), heavy T2W SE, T2W gradient echo (GRE), T1W in-/opposed phase spoiled gradient recalled (SPGR) echo, and diffusion weighted images (DWI). Additional coronal plane MRIs were performed using single-shot fast-spin echo T2W. Gd-EOB-DTPA (Primovist®) was administered by injection at a recommended dose of 0.1 mmol/kg, and a flow rate of 2.0 mL/second. The MRI pulse sequence was axial 3D fast SPGR with fat suppression. Scanning was performed during the arterial phase (25-30 seconds post-injection, portal venous phase (70-90 seconds post-injection), and several delayed phases at 3, 5, and 10 minutes' post-injection. The hepatobiliary phase was the final routinely delayed phase, at 20 minutes, and 40 minutes in severe cirrhotic livers.

Data management and analysis

Data were retrieved from the Hospital 2000 System archive and summarized into Case Report Forms (CRF). Imaging reports were read and interpreted from the Hospital's Picture Archiving and Communication Systems (PACS). Descriptive statistics for proportions, means and standard deviations were used to describe the data. Intercooled Stata or Stata/SE version 9.2 (StataCorp, College

Station, TX, USA) was used for data analysis. Proportions were compared using Pearson's Chi-square (χ^2); the one-way ANOVA test was used to compare means, and statistical significance was set at $\alpha = 0.05$.

Results

The medical records of 19 patients showed that their mean age (±SD) was 46.3 (±15.5) years; 8 (42.1%) were females; 9 (47.4%) were cirrhotic, 8 (42.1%) had benign lesions, and 11 (57.9%) had malignant lesions. Of 15 available blood samples, 4 (26.7%) had hepatitis B virus (HBV) antibody, 2 (13.3%) had hepatitis C virus (HCV) antibody, and 3 (20.0%) had both. Of the 21 lesions available for review, 12 (57.1%) were benign. Mean (±SD) of nodules is 4.4 (± 4.2) cm. (median = 3 cm). The difference in percentage Primovist® uptake in the hepatobiliary phase of the cirrhotic (mean ± SD = 65.0 ± 30.0%) and non-cirrhotic (mean ± SD = 87.6 ± 21.1%) cases was not statistically significant (p = 0.09).

Contrast studies were divided into two parts. The dynamic contrast studies had 4 enhancement patterns, *i.e.* centripetal (4.8%), hypervascular (71.4%), hypovascular (14.3%) and no enhancement (9.5%). In the hepatobiliary (HB) phase, the Primovist® hepatocyte uptake pattern was classified into 3 groups, i.e., no uptake (61.9%), partial uptake (23.8%), and total uptake (14.3%).

Of 9 benign nodules, 4 were hepatic adenomas, of which 2 had underlying renal-cell carcinoma, and breast cancer. Of the remaining 5 benign nodules, 2 were hemangiomas, one was a porto-hepatic venous malformation, one was a nodular reactive hyperplasia (NRH), and one was an atypical FNH. Of 12 malignant nodules, 10 were HCC, and 2 were metastases from known rectal and bladder cancers.

Table 1 re-categorizes the above diagnoses into 4 groups--HCC, FNH/HA, metastatic lesions, and others, and compares them with hepatobiliary-phase uptake patterns, showing any significant association (p = 0.02). Most HCCs (80%) showed no uptake pattern for Primovist®.

Table 2 shows a comparison between mean percentage enhanced nodules during the hepatobiliary phase among different diagnoses, where significant differences were observed (p <0.01). Among these, only degree of contrast enhancement between HCC and FNH/HA showed any significant mean difference (60.7%; p =0.03). Other pairwise comparisons showed non-significant differences (p >0.06 for any comparison).

Six cases with remarkable characteristics are described, as follows.

Case 1 was a 46-year-old man who presented with an exophytic mass in segment 5 of the right hepatic lobe detected incidentally by sonography. AFP level was normal (2.9 ng/mL.), and both HBV and HCV antibodies were negative. The mass was eventually resected and showed well-differentiated HCC.

The first MRI of the upper abdomen was performed using conventional gadolinium chelate agent (Figures 1A-G). Figures 1A and B were in-/opposed phase SPGR pulse sequence, showing signal loss of the mass on the opposed phase, indicating intracellular lipid component. Figure 1C was T2W with fat suppression, demonstrating a hyperintense central scar within the mass. Figures 1D-G are pre- and post-contrast arterial, portal venous, and delayed phases, showing rapid arterial enhancement with some wash-out on the porto-venous phase, and delayed central scar enhance-

A.

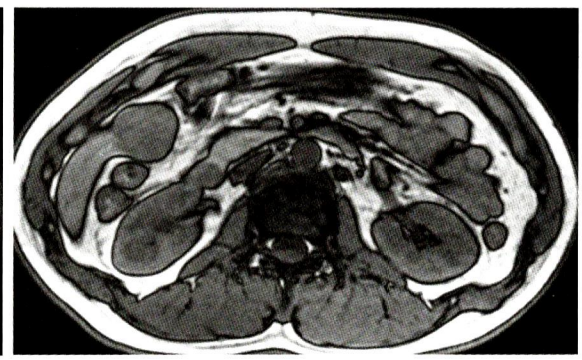

B.

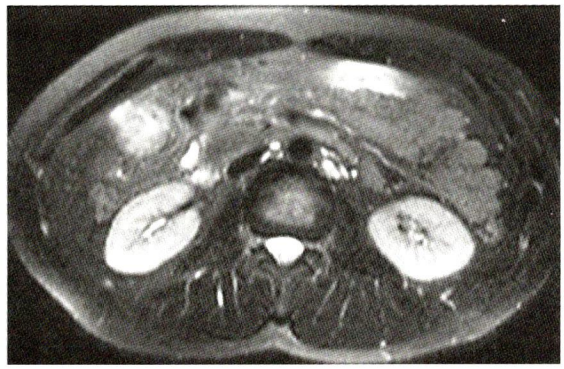

C.

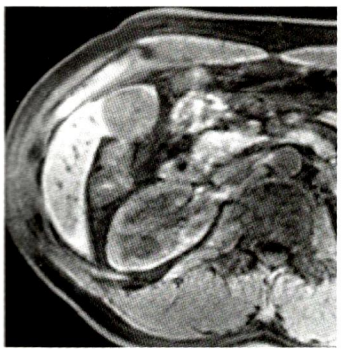

D.

E.

F.

G.

Case 1: Exophytic HCC mimics FNH

Fig.1 A-G MRI of upper abdomen with conventional gadolinium

A. In phase
B. Out of phase SPGR
C. T2W fat suppression
D. Plain
E. Arterial
F. Portovenous
G. Delayed phase

Table 1 Description of final diagnoses compared with uptake patterns in different hepatobiliary phases

Hepatobiliary phase	HCC	FNH/HA	Metastases	Others	Total
Non-uptake	8	0	2	3	13
Partial Uptake	2	2	0	1	5
Total Uptake	0	3	0	0	3
Total	10	5	2	4	21

Pearson's χ^2 (p =0.021)

Table 2 Comparison between mean percentages of enhanced nodules during hepatobiliary phase among different diagnoses

Final diagnosis	Percent enhanced nodule		
	Mean	Standard deviation	Frequency
HCC	44.9	26.4	10
FNH/HA	105.6	28.0	5
Metastases	30.8	16.8	2
Others	104.8	60.0	4

One-way ANOVA test (p <0.01)

ment. These MRI findings were more favorable for focal nodular hyperplasia (FNH) than HCC. However, the exophytic appearance is atypical for FNH, and HCC was still possible.

Therefore, the second MRI was performed with liver-specific contrast agent (Primovist®). Figures 2A-D are pre- and post-contrast arterial, venous, and 20 min delayed hepatobiliary (HB) phase scans. The enhancement pattern was similar to conventional gadolinium, but with more information on the HB phase. The mass showed no Primovist® uptake (D), indicating no functioning hepatocytes, so that it was unlikely to be FNH. The hypervascular mass with no Primovist® uptake was likely to be HCC. Surgery was later performed with wedge resection of the mass, and cholecystectomy (Figure 3A). Pathological diagnosis (Figure 3B) revealed well-differentiated hepatocellular carcinoma, with a trabecular pattern and positive staining for CD34. The mass showed a large number of sinusoids without vascular invasion.

Case 2 was a 51-year-old woman with underlying chronic hepatitis B and cirrhosis, who presented with high AFP, 500 ng/ml. MRI with HB-specific contrast enhancement (Primovist®) showed a nodule-within-a-nodule appearance in segment 7 of the right hepatic lobe. The central nodule showed low signal intensity (SI) at T1W, high SI at T2W, and rapid arterial enhancement with no uptake in the delayed HB phase (Figures 4A-F). Findings were consistent with early HCC. She underwent transarterial chemoembolization (TACE) treatment. The angiogram during treatment showed a small hypervascular mass supplied by branches of the right hepatic artery, confirming a diagnosis of HCC (Figures 4G-H). A plain post-treatment CT confirmed lipiodol staining within the tumor (Figures 4I).

Case 3 was a 69-year-old man, with negative HBV and HCV antibodies, a normal AFP level of 6.7

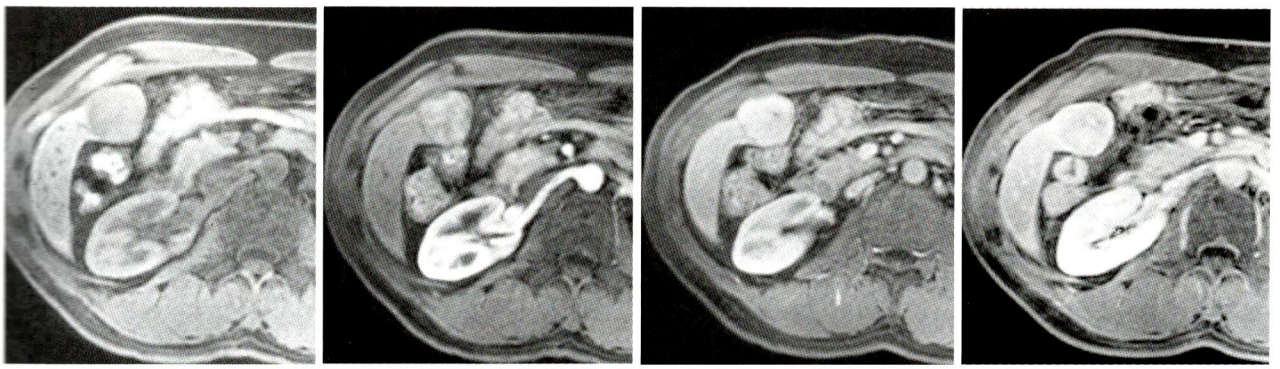

A. B. C. D.

Case 1: Exophytic HCC mimics FNH

Fig.2 A-D MRI of the upper abdomen with hepatocyte-cell-specific agent using Primovist®.

A. Plain

B. Arterial

C. Portovenous

D. Hepatobiliary phase, 20 minutes p.i.

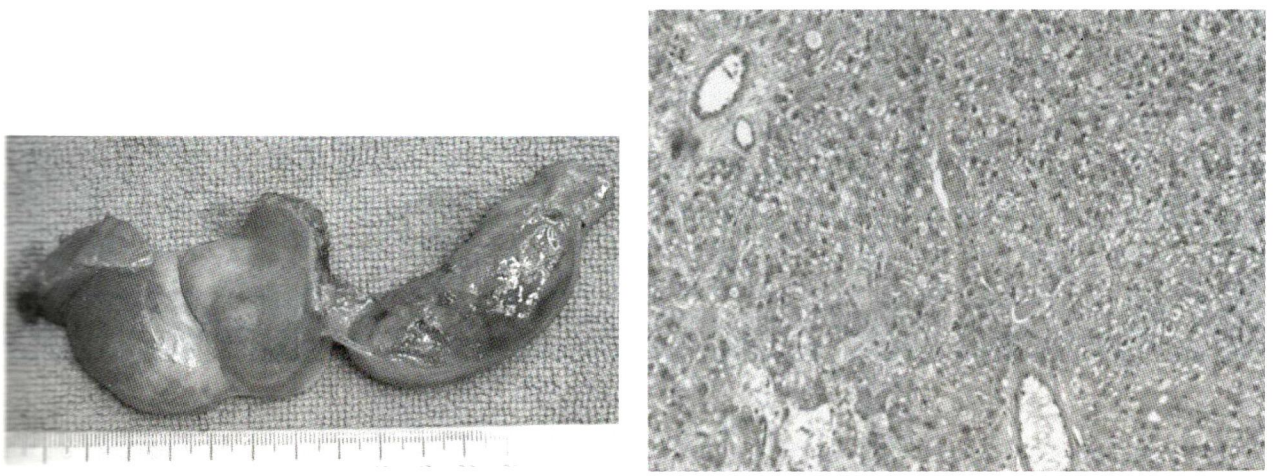

A. B.

Case 1: Exophytic HCC mimics FNH

Fig.3 A-B Gross and histological specimens after wedge resection of the liver and cholecystectomy

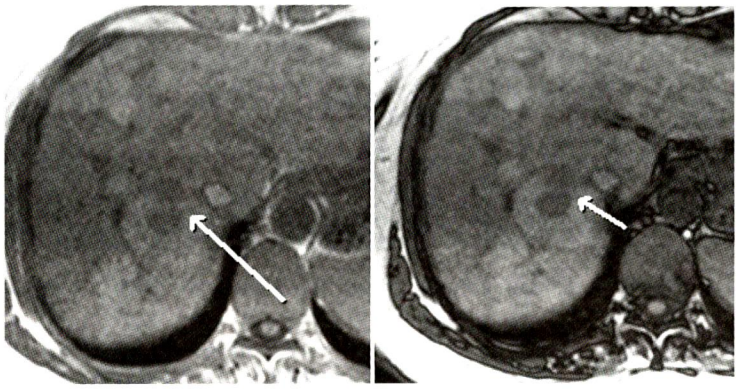

A. In and out of phase spoiled gradient echo [recalled] (SPGR)

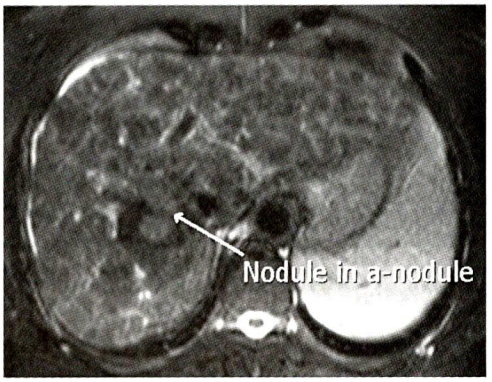

B. Axial T2W with fat suppression appears as high signal on T2W of a couple of mural nodules, showing the nodule-within-a-nodule pattern.

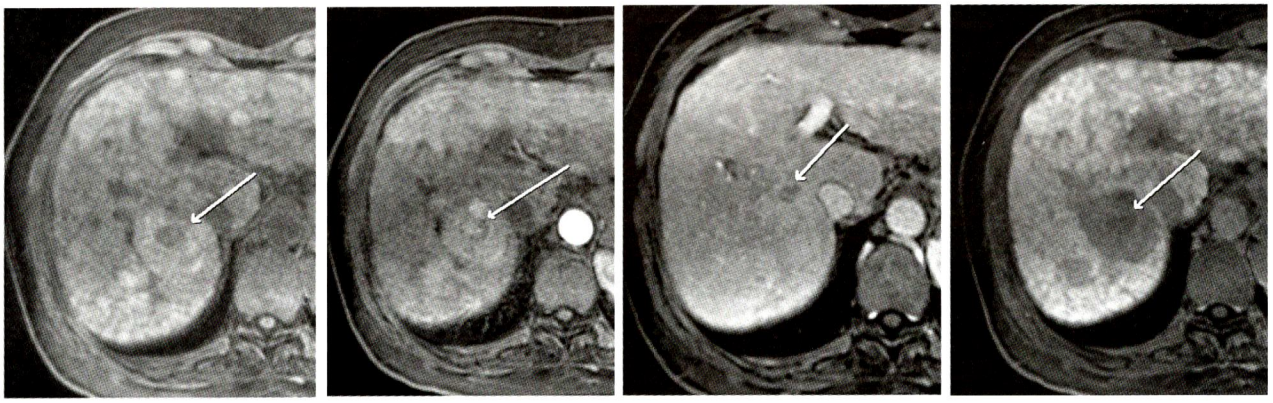

C. D. E. F.

Dynamic contrast enhancement (DCE) study with Gd-EOB-DTPA demonstrates rapid nodular enhancement on the arterial phase (D), rapid wash-out on portovenous phase (E), then 20-minute delay p.i, and hepatobiliary phase (HB phase; F). The mural hypervascular nodules and the large main, non-enhancing hypersignal T1/hyposignal T2 dysplastic nodule become dark with low signal, reflecting absence of hepatocyte-cell components and/or hepatocyte-cell dysfunction.

Fig.4 A-I

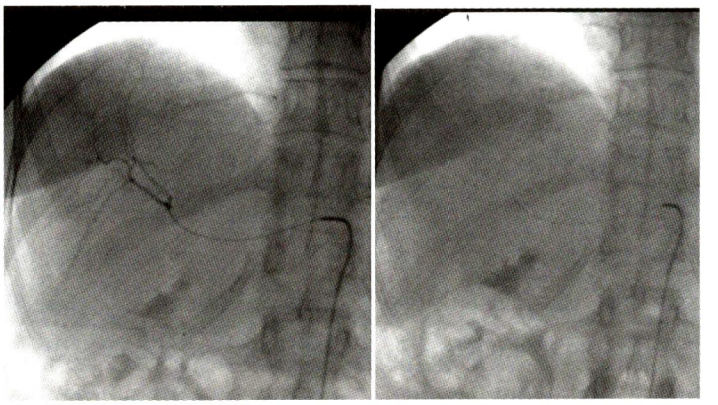

G.

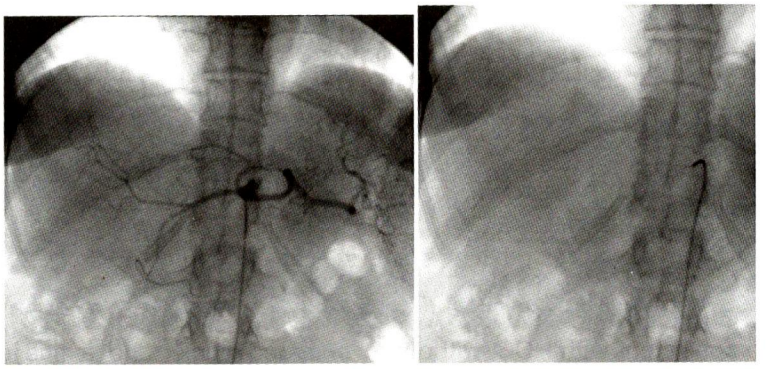

H. Angiograms during treatment show a small hypervascular mass supplied by branches of the right hepatic artery, confirming a diagnosis of HCC (G, H).

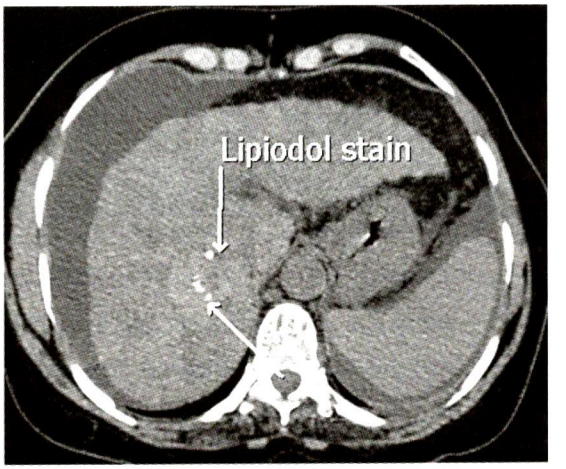

I. CT Demonstration of post first TACE treatment, 2-3 months after the early HCC, with evidence of residual small lipiodol uptake at the lesion. These findings are consistent with small HCC, with some treatment effect.

Fig.4 A-I *(cont.)* Primovist®-enhanced MRI study (Case 2)

ng/mL., and CEA of 2.1 ng/mL. A liver tumor mass of 2.7 cm, with fatty metamorphosis was found, with moderate signal intensity T2W. A dynamic contrast study (DCE) showed a hypervascular pattern (40.43% enhancement increase), with rapid wash-out. The hepatobiliary-phase Primovist®-enhanced study showed hypointense non-Primovist® uptake (19.15%), indicating the absence of hepatocyte cells. A Kupffer-cell-specific phase double-contrast study revealed hyperintensity on T2W and gradient-echo (GRE) T2W, indicating non-iron uptake and absence of Kupffer cells (Figures 5A-D). MRI with Gd-EOB-DTPA (hepatocyte cell specific agent-Primovist®) demonstrated hypervascularity on the hepatic arterial phase (HAP) with hypointense and non-hepatocyte uptake on hepatocyte-selective phase, indicating the absence of any hepatocyte component. All of these radiologic findings are consistent with HCC, without hepatocyte and Kupffer cell components, which was consistent with the pathological findings appearing as diffused fatty change and focal cellular atypia of hepatocytes.

Case 4 was a 39-year-old woman with a liver mass on sonographic check-up and normal AFP level (1.9 ng/mL); hepatic adenoma needed to be ruled out. Her hepatocyte-specific MRI of the upper abdomen demonstrated a right hepatic nodule appearing hyposignal T1 and pre-contrast axial 3-D signals (Figures 6A-6C) and mild hypersignal T2 (Figure 6B) intensity, with rapid wash-in on HAP (Figure 6D). Enhancement remains on both portal venous phase (PVP) and venous phase (Figure 6E). During the hepatobiliary phase (Figure 6F), the partial hepatocyte uptake in the peripheral portion indicates the presence of hepatocyte cells. These favor a benign hypervascular nodule, probably due to focal nodular hyperplasia or less-likely hepatic adenoma. Another MRI of the upper abdomen was performed (figures not shown) using the Kupffer-cell-specific liver agent, Super Paramagnetic Iron Oxide (SPIO-Resovist®, Bayer Schering Pharma AG, Leverkusen, Germany). The nodule exhibited tiny foci with dark signal internally, probably due to minute Kupffer cell components, in a similar pattern to the partial hepatocyte uptake in the gadoxetic-acid study. A follow-up MRI 3 months later revealed a slight decrease in size and enhancing area of the pre-existing hypervascular tumor at the posterior right lobe. This event followed discontinuation of oral contraceptive 3 months earlier, with some evidence of a hepatocyte component that was likely benign, such as focal nodular hyperplasia (FNH) or hepato-cellular adenoma (HA). Histopathology found small clusters of near-normal liver cells with slightly enlarged nuclei and a fine chromatin pattern and distinct nucleoli, compatible with focal nodular hyperplasia and/or liver-cell adenoma (Figure 7).

Case 5 was a 33-year-old woman with a hypersignal T2 right hepatic nodule in segments 5 and 6, with characteristically increased hyperintensity on heavy T2W (Figure 8A). Dynamic contrast enhancement (DCE) studies using Gd-chelate agent injection demonstrated the characteristic centri-petal enhancement pattern of the hemangioma, from HAP, PVP, and delayed scans until 10 minutes p.i. (Figures 8B-E). DCE using gadoxetic agent (Gd-EOB-DTPA/gadoxetic agent) demonstrated centrip-etal pattern of characteristic hemangioma on HAP, PVP and delayed 3 minutes p.i. On the HB phase (20 minutes), it turned into total low-signal intensity, reflecting non-hepatocyte uptake from the absence of any hepatocyte component in the hemangioma (Figures 8F-I).

Case 6 was a 58 year-old man, a known-

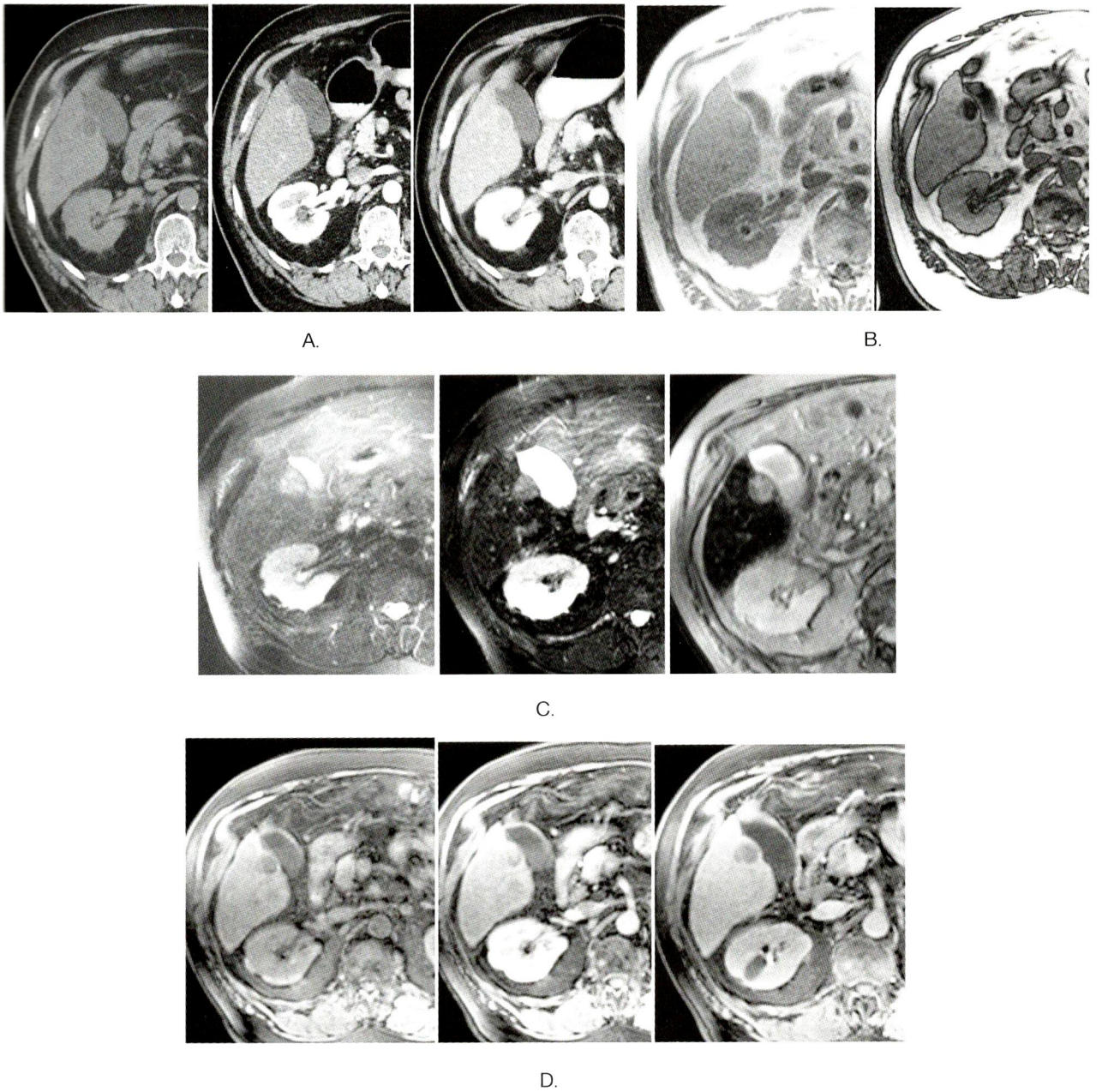

Fig.5 A-D Multi-Detector Computerized Tomography (MDCT), Case 3

A. MDCT of upper abdomen, plain, hepatic arterial phase (HAP) and portovenous phases (PVP) plus iodinated contrast media demonstrate hypervascular nodule at peripheral hepatic segment V, abutting the gall bladder fossa.

B. Chemical shift imaging, in and out of SPGR phases, representing fatty component or fatty metamorphosis

C. T2W T2W plus SPIO GRE T2W plus SPIO MRI with Super Paramagnetic Iron Oxide (SPIO-a Kupffer-cell-specific liver agent) demonstrating non-iron uptake of this nodule, indicating absence of the Kupffer cell component.

D. Plain HAP plus Primovist® HB phase plus Primovist®

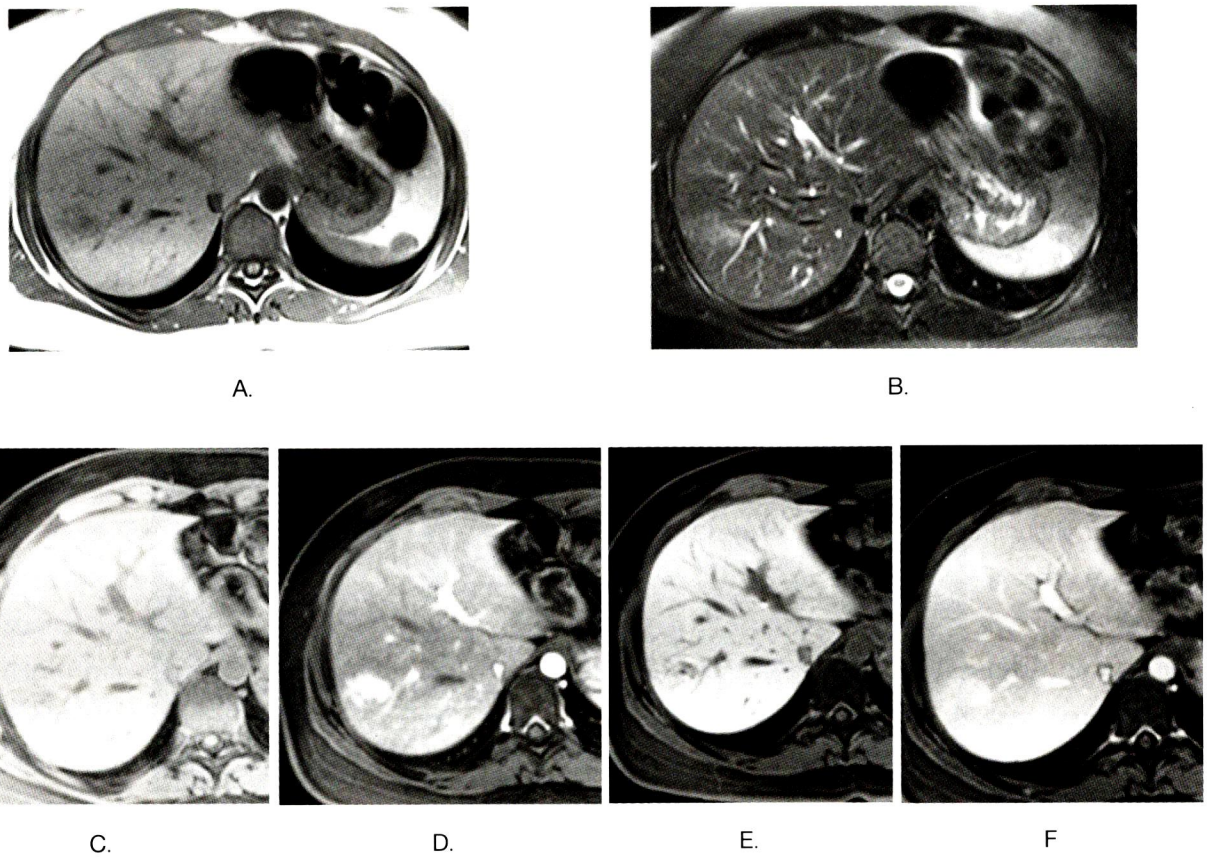

Fig.6 A-F MRI of the upper abdomen (Case 4)
A. In-phase SPGR
B. T2W fat sat
C. Plain
D. Arterial phase
E. Portovenous phase
F. HB Phase, 20 minutes after Primovist® agent

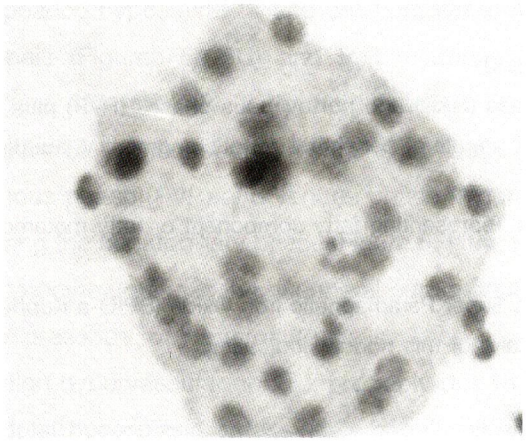

Fig.7 Pathological section of liver (Case 4) showing small clusters of near-normal liver cells with slightly enlarged nuclei with fine chromatin pattern and distinct nucleoli, compatible with focal nodular hyperplasia and/or liver-cell adenoma

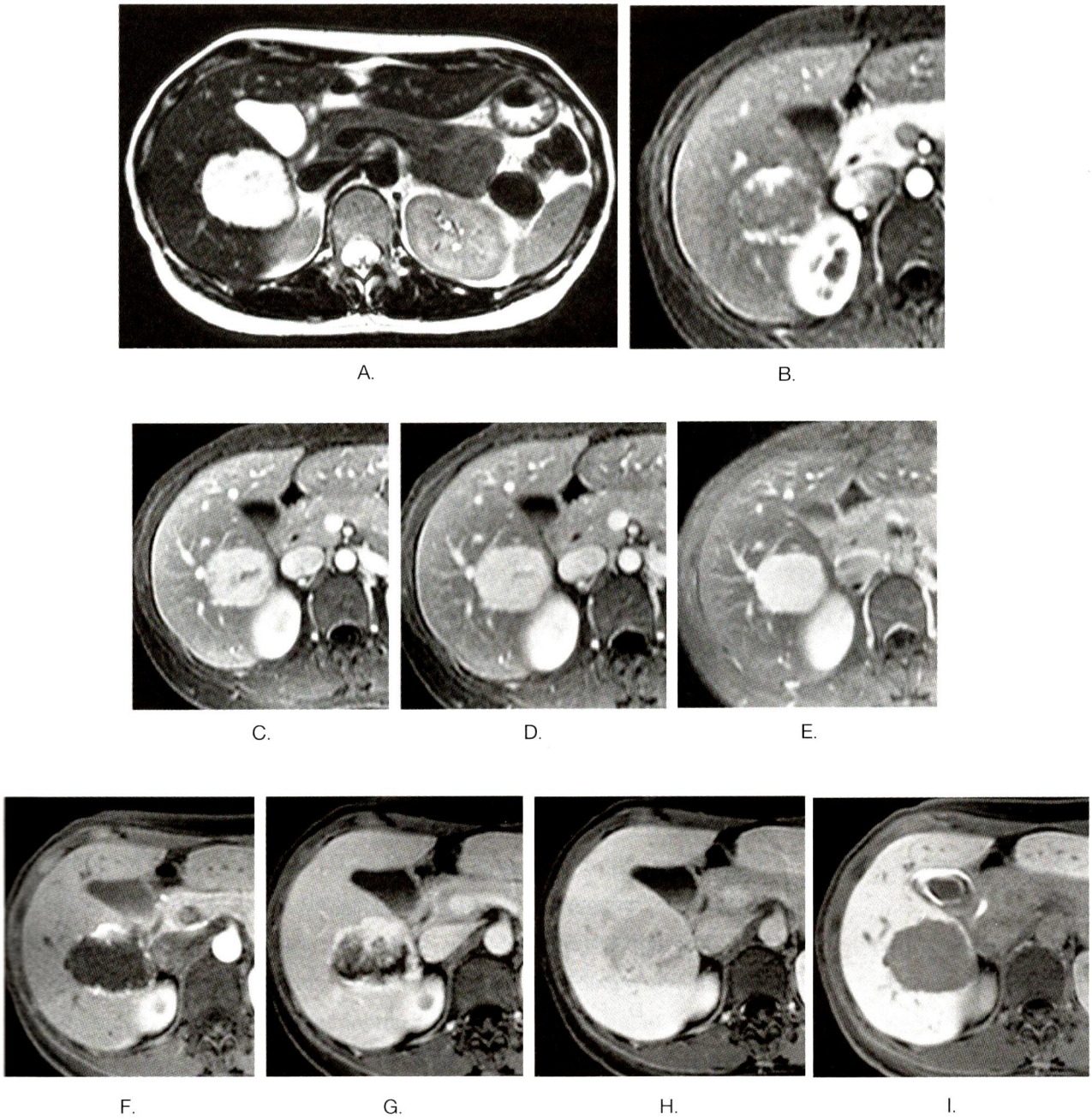

Fig.8 A-I Radiologic findings of Case 5 (hemangioma)

A. Axial heavy T2W

B. HAP

C. PVP

D, E Delayed 3 and 10 minutes after Gadolinium agent

F. HAP plus Primovist®

G. PVP plus Primovist®

H, I Delayed 3 minutes and HB phase 20 minutes p.i

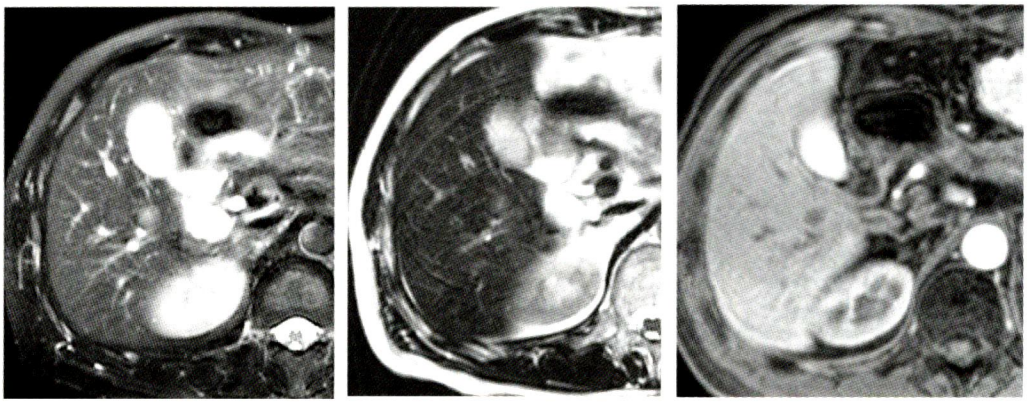

A. B. C.

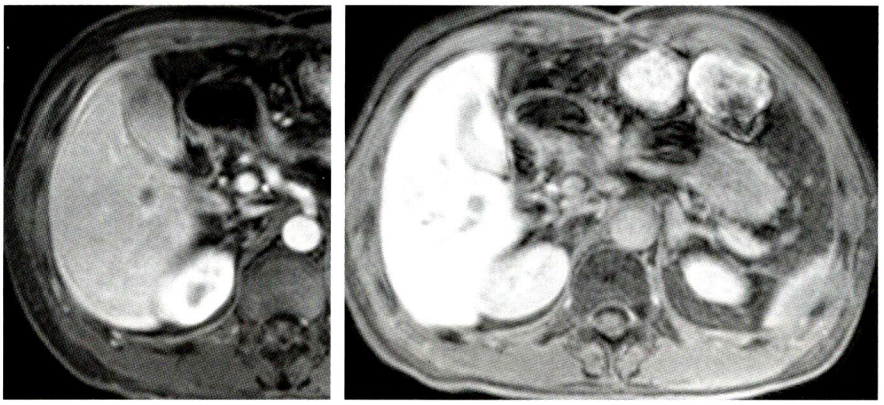

D. E.

Fig.9 A-E MRI findings of Case 6

A. T2W Fat suppression technique
B. Heavy T2W
C. DCE:HAP
D. PVP plus Primovist®
E. HB phase at 20 minutes p.i

case of rectal cancer with hypovascular liver nodules. He was studied with Primovist®-enhanced MRI of the upper abdomen, appearing in a non-hepatocyte pattern suggestive of hypovascular liver metastasis (Figures 9A-E).

The remaining 17 lesions were diagnosed and concluded by clinical history, AFP, and periodic follow-up studies over 2-4 years.

For the record, no adverse drug reaction or undesirable effect was observed after intravenous Primovist® injection in this study, nor even minor drug reactions, such as rash, erythema, nausea, or vomiting.

Discussion

This study describes the magnetic resonance imaging (MRI) findings for different liver masses using Gd-EOB-DTPA as an intravenous contrast

agent. In addition to imaging findings from routine MR sequences and dynamic contrast studies, uptake patterns during the hepatocyte-specific phase can provide additional information and help characterize liver masses.

In the present study, about 80% of all cases showed typical HCC characteristics, including hypervascular patterns, hypersignal T2 intensity, and hypointense nodules due to non-hepatocyte uptake in the hepatocyte-selective phase. About 20% showed an atypical pattern, including partial hepatocyte and cell component uptake, resulting in mimicking and misdiagnosing as FNH, HA, or adenomatosis, in non-cirrhotic livers and high grade dysplastic nodules in cirrhotic livers. For example, the non-cirrhotic and indeterminate ones finally proved to be well-differentiated HCC, which also exhibited normal AFP levels, first an FNH-like pattern (as delayed enhanced hypersignal T2 central scar after extracellular gadolinium chelate agent) and slow growth in the subsequent year, but with non-hepatocyte uptake after Gd-EOB-DTPA, which was atypical of FNH. Thus, tissue diagnosis is strongly recommended to rule out such conditions.

For benign hypervascular nodules, the liver nodule/nodules showed homogeneous rapid enhancement on HAP, rapid wash-out on PVP after routine Gd study, iso to slightly hyper/hyposignal T1W and T2W, reflecting a hypervascular pattern found in many diseases, such as focal nodular hyperplasia (FNH), hepatic adenoma (HA), liver adenomatosis, hepatocellular carcinoma (HCC), and hypervascular metastases. Computed tomography cannot well differentiate these lesions. Therefore, MRI of the upper abdomen yields improved detectability and tissue characteristics. Hepatocyte-cell-specific enhanced MRI can usefully differentiate FNH from other lesions, including HA, hypervascular metastases, and most HCCs, by evaluating the presence of uptake and non-uptake in the HB phase in 15-20 minutes post-injection, respectively. Central scars are a typical characteristic, that becomes hypointense/non-uptake in HB phase and the presence of central high signal on T2W. In this study, Table 2 shows percentage hepatocyte uptake in the HB phase for various groups, including HCC, FNH/HA, and metastases. It is important to note that there were significant characteristics between hepatocyte uptake in HCC and FNH/HA. Therefore, the hepatocyte-selective phase is useful for characterization. Unfortunately, liver metastases cannot be assessed satisfactorily because of the inadequate sample size. Primovist®-enhanced MRI is feasible and robust for diagnosing typical FNH. It has a typical enhancement pattern under Gd-EOB-DTPA contrast, in both hypervascular pattern in dynamic contrast studies, and significant hepatocyte/contrast uptake plus focal non-uptake of the characteristic hypersignal T2 central scars in the 20-minute-delayed hepatocyte-selective phase.

Regarding hepatic hemangiomas and the findings in hepatocyte-cell-specific MRI studies, *i.e.*, a finding of hypointensity with no hepatocyte uptake, mimicking a malignancy pattern, can frequently result in misdiagnosis and inappropriate treatment. Some of these cases may incorrectly be referred to interventional therapy or tissue biopsy. Clarification is simple, by one more acquisition, a heavy T2W sequence. Hemangiomas demonstrate moderate to markedly hyperintense or bright up-signal intensity, in a pattern like a light-bulb. In addition, on triple phase and 3-minutes delayed p.i, it exhibits a characteristic centripetal pattern, *i.e.*, early peripheral nodular enhancement on HAP, gradually delayed

and increasing, and persistent enhancement on later delayed phases. In this study, the complete centripetal pattern was identified on 3-minute p.i, while hepatocyte-cell uptake starts at 5 minutes p.i, so that a hemangioma gradually becomes darker, with low signal intensity and non-hepatocyte uptake.

Since no metastatic liver nodules have a hepatocyte cell component, both hyper- and hypovascular nodules show hypointensity in the hepatobiliary phase. Gd-EOB-DTPA can improve detectability, which is useful for the planning of therapeutic and surgical management strategies. Hepatocellular adenoma and HCC both show hypervascularity and similar patterns for a wide variety of hepatocyte cell components, resulting in various patterns from non-uptake to high uptake of this contrast agent; this can cause interpretation problems. The characterization and differentiation of hepatocellular adenoma and HCC are only clear in the hepatobiliary phase. The internal content of fat and hemorrhage can also be found in both situations. Since nodular reactive hyperplasia or perfusion abnormalities were found in this study, hypervascular pseudolesions can be differentiated from true hepatocellular nodules by isointensity in a plain MRI, both in T1W and T2W. In some cases, however, these mimic FNH or hepatic adenomas. Gadoxetic acid provides the special characteristics of total contrast uptake and the presence of hepatocyte cell components.

The present study had some limitations. First, the sample size was small. Second, the number of histopathologically proven cases was small. The study, however, had periodic follow-up for 2-3 years, with stability in the case of benign liver nodules, post-treatment response or progression in liver metastases, and post-therapy change or growth of tumor and amount of lipiodol uptake following TACE or radiofrequency ablation. Third, some diagnoses were few in number, so that the imaging findings may not adequately represent the majority.

In conclusion, MRIs of the liver with a hepatocyte-cell-specific agent is a useful tool for the detection and characterization of focal liver lesions, particularly in the diagnosis of FNH. They can be helpful in HCC, and high-grade dysplastic nodules with highly malignant potential on the underlying cirrhotic liver, to differentiate low risk nodules, such as low-grade dysplastic and regenerating nodules. This type of study is also helpful in liver metastases, especially for detectability and the differentiation of multiple liver nodules from hepatocellular-containing nodules, such as multifocal HCCs. However, there are also some limitations for well-differentiated or hepatocyte-containing HCC, HA, hepatic adenomatosis and atypical tiny hemangiomas with marked delayed enhancement. Therefore, an evaluation of the findings for other MRI techniques-T1W, in-/out phase chemical shift sequence, T2W, heavy T2W, and diffusion-weighted imaging-would also be helpful.

Acknowledgments

This study was supported by Bayer Thai Co. Ltd., who provided the MRI contrast agent. None of the authors is an employee of the sponsor. The authors have full control of the data and information for publication. Thanks to Dr. Sith Phongkitkarun and Dr. Linda Pantongrag-Brown for their critiques on the manuscript, and Dr. Dwip Kitayaporn and Ms. Natchayada Tanabvonnon of Bumrungrad International Clinical Research Center (BI/CRC) for technical advice and other support.

References

1. Bellin MF, Vasile M, Morel-Precetti S. Currently used non-specific extracellular MR contrast media. Eur Radiol 2003;13:2688-98.
2. Reimer P, Schneider G, Schima W. Hepatobiliary contrast agents for contrast-enhanced MRI of the liver: properties, clinical development and applications. Eur Radiol 2004;14:559-78.
3. Karabulut N, Elmas N. Contrast agents used in MR imaging of the liver. Diagn Interv Radiol 2006;12:22-30.
4. Gandhi SN, Brown MA, Wong JG, Aguirre DA, Sirlin CB. MR contrast Agents for Liver Imaging: What, When, How. Radiographics 2006;26:1621-36.
5. Shellock FG, Kanal E. Safety of magnetic resonance imaging contrast agents. J Magn Reson Imaging 1999; 10: 477-84.
6. Semelka RC, Helmberger TK. Contrast agents of MR imaging of the liver. Radiology 2001;218:27-38.
7. Huppertz A, Balzer T, Blakeborough A, Breuer J, Giovagnoni A, Heinz-Peer G, et al. Improved detection of focal liver lesions at MR imaging: multicenter comparison of gadoxetic acid-enhanced MR images with intraoperative findings. Radiology 2004;230:266-75.
8. Hecht EM, Holland AE, Israel GM, Hahn WY, Kim DC, West AB, et al. Hepatocellular carcinoma in the cirrhotic liver: gadolinium-enhanced 3D T1-weighted MR imaging as a stand-alone sequence for diagnosis. Radiology 2006;239:438-47.
9. Yu JS, Cho ES, Kim KH, Chung WS, Park MS, Kim KW. Newly developed hepatocellular carcinoma (HCC) in chronic liver disease: MR imaging findings before the diagnosis of HCC. J Comput Assist Tomogr 2006;30:765-71.B.
10. Vogl TJ, Kümmel S, Hammerstingl R, Schellenbeck M, Schumacher G, Balzer T, et al. Liver tumors: comparison of MR imaging with Gd-EOB-DTPA and Gd-DTPA. Radiology 1996;200:59-67.
11. Reimer P, Schneider G, Schima W. Hepatobiliary contrast agents for contrast-enhanced MRI of the liver: properties, clinical development and applications. Eur Radiol. 2004; 14:559-78.
12. Reimer P, Rummeny EJ, Shamsi K, Balzer T, Daldrup HE, Tombach B, et al. Phase II clinical evaluation of Gd-EOB-DTPA: dose, safety aspects, and pulse sequence. Radiology 1996;199:177-83.
13. APRN Newsletter. Ministry of Public Health, Food and Drug Administration. http://www.fda.moph.go.th/fda-net/html/product/apr/newsletter/APRNewsletter__gadolinium__.pdf - accessed 27/09/2007.
14. Sakamoto M, Hirohashi S, Shimosato Y. Early stage of multistep hepato-carcinogenesis: adenomatous hyperplasia and early hepatocellular carcinoma. Hum Pathol 1991; 22:172-8.
15. Choi BI, Takayasu K, Han MC. Small hepatocellular carcinomas and associated nodular lesions of the liver: pathology, pathogenesis, and imaging findings. AJR AM J Roentgenol 1993;160:1177-87.
16. Ferrell LD, Crawford JM, Dhillon AP, Scheuer PJ, Nakanuma Y. Proposal for standardized criteria for the diagnosis of benign, borderline, and malignant hepatocellular lesions arising in chronic advanced liver disease. Am J Surg Pathol 1993;17:1113-23.
17. Sadek AG, Mitchell DG, Siegelman ES, Outwater EK, Matteucc T, Hann HW. Early hepatocellular carcinoma that develops within macroregenerative nodules: growth rate depicted at serial MR imaging. Radiology 1995;195: 753-6.
18. Hamm B, Staks T, Mühler A, Bollow M, Taupitz M, Frenzel T, et al. Phase I clinical evaluation of Gd-EOB-DTPA as a hepatobiliary MR contrast agent: safety, pharmacokinetics, and MR imaging. Radiology 1995;195:785-92.
19. Jung G, Breuer J, Poll LW, Koch JA, Balzer T, Chang S, et al. Imaging characteristics of hepatocellular carcinoma using the hepatobiliary contrast agent Gd-EOB-DTPA. Acta Radiol 2006;47:15-23.
20. Elsayes KM, Narra VR, Yin Y, Mukundan G, Lammle M, Brown JJ. Focal hepatic lesions: diagnostic value of enhancement pattern approach with contrast-enhanced 3D gradient-echo MR imaging. Radiographics 2005;25: 1299-320.

THE **ASEAN JOURNAL** OF **RADIOLOGY** 2012: 18(3): 184-188

Case Report

Colitis Cystica Profunda Mimicking Mucinous Adenocarcinoma of Colon; A Case Report

Luckana Girapongsa MD.[1], **Polchai Malaipornpong MD.**[2], **Orawan Autravisitkul MD.**[1], **Pariyanoot Deesuwun MD.**[1]

Department of Radiology[1], *Samutsakhon Hospital, Samutsakhon, Thailand. Department of Surgery*[2], *Samutsakhon Hospital, Samutsakhon, Thailand.*

Abstract

Colitis cystica profunda (CCP) is a rare benign disorder characterized by the mucus collection in the submucosal layer of the colon. The most common type is localized type predominate at the rectosigmoid colon. It may be mimic carcinoma of the colon leading to unnecessary surgery. We present a case of colitis cystica profunda segmental type at the ascending colon and the caecum mimicking mucinous adenocarcinoma of colon.

Keyword: Colitis cystica profunda, CA colon, submucous cyst.

Introduction

Colitis cystica profunda (CCP) is a rare benign condition.[1,2,5] There have been 200 cases of CCP reported in the literature.[1] Stark first reported two autopsied cases of CCP accompanied by chronic dysentery in 1766.[10] Virchow introduced the term "colitis cystica polyposa." in 1863[11] The etiology is unclear. The lesion is characterized by mucin-filled submucosal cysts lined with normal colonic epithelial cells.[3] It may be mimic carcinoma of the colon from both radiologic and pathologic standpoint.[4,6] Our case is a case of colitis cystica profunda mimicking mucinous adenocarcinoma of colon.

Case report

History

A 57-years-old male presented with abdominal distension and frequency in loose stool for 5 months ago. The physical examination revealed ill-defined palpable mass at RLQ area measuring about 10 cm in size and showed no tenderness.

The vital sign ; T 38.4°c, PR 128/min, RR 22/min, BP 120/70 mmHg. The CBC; Hemoglobin 12.4 g/dl (normochronic normocytic appearance), WBC 12,400 cell/uL (neutrophil 78.4%) and platelet count 313,000 cell/uL. His laboratory investigation including kidney and liver function test were within normal limited.

Then he performed the computed tomography of the whole abdomen. The computed tomographic findings revealed large ill-defined irregular low attenuation lesion at the posterior wall of the caecum and the ascending colon continuing with evidence of abscess formation at the right-side of the retroperitoneum surrounding by some subcentrimeter pericolic lymph nodes.

The preliminary diagnosis was ruptured mucinous adenocarcinoma of the colon with abscess in right retroperitonum.

The CT finding of the whole abdomen

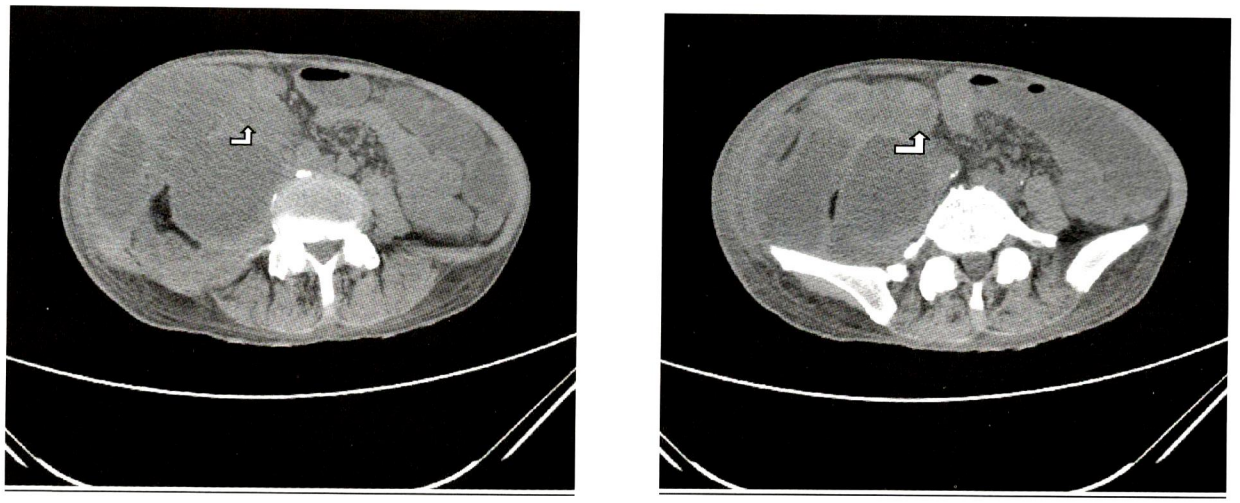

A B

Fig.1 A,B Non-contrast study revealed irregular ill-defined low attenuation lesion at the posterior wall (curve arrow) of caecum and ascending colon.

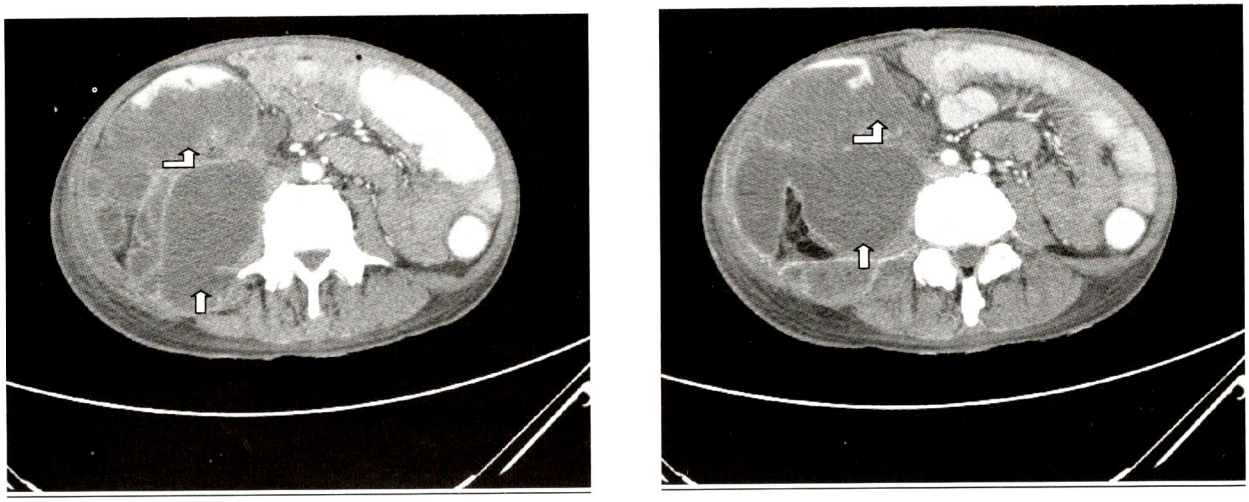

A B

Fig.2 A,B In arterial phase, the posterior wall lesion (curved arrow) showed homogenous hypoattenuation continuing to the large fluid-density lesionsurrounding by rim-enhancement (straight arrow); representing abscess in the right retroperitoneum.

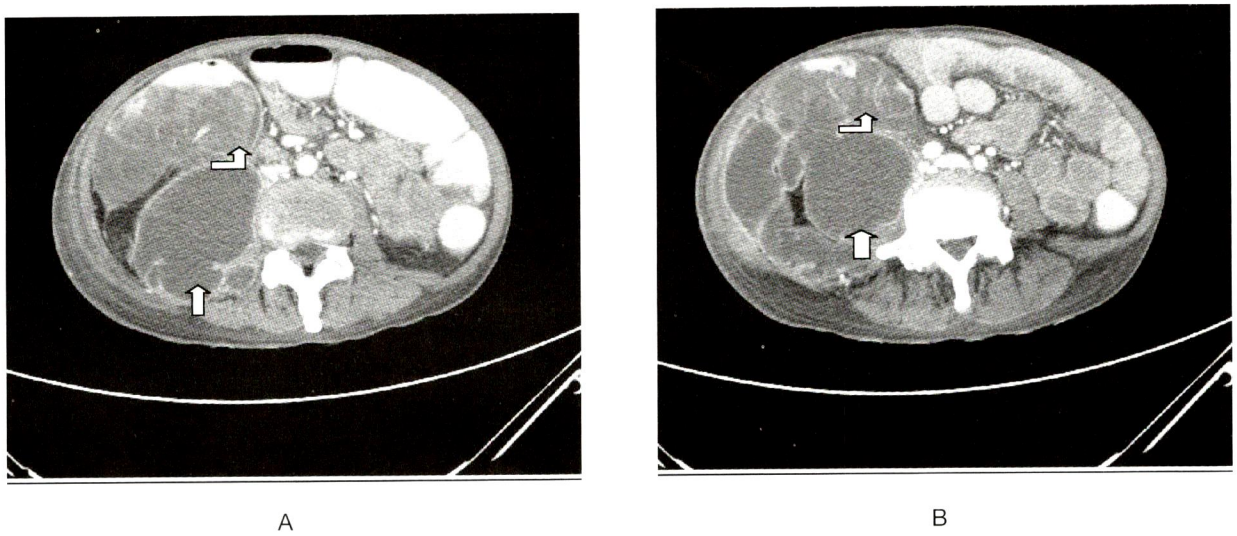

A B

Fig.3 A,B In the portal phase, the posterior wall lesion(curved arrow) showed slightly heterogeneous increased attenuation continuing to right retroperitoneal abscess (straight arrow).

Then he was explored laparotomy with performing right hemicolectomy and finally his tissue diagnosis was chronic active colitis and changes consistent with colitis cystic profunda. No granulomas or viral inclusions are seen. No evidence of malignancy is noted.

Discussion

Colitis cystica profunda (CCP) is a rare benign disorder of the colon and the rectum.[1,2,5] The etiology is not clear. Two theories have proposed to explain the etiology of CCP. Firstly, there is a congenital malformation consisting of colonic mucosal glands growing into submucosa. Secondary, there is herniation of colonic mucosa accounting for congenital or acquired defect of muscularis mucosae. It has been postulated that abnormal muscle contraction may force the glands into the submucosa with implicated by radiation, ischemia and physical trauma.[2] There is generally agreement that CCP results from mucosal inflammation and ulceration.[5,6]

The most common presenting symptoms are feces with mucus, rectal bleeding, rectal tenesmus, dyschezia , proctalgia fugax , alters bowel habit and a long history of obstructive defecation.[2,5] In this case, the presenting symptoms were abdominal distension and frequency in loose stool.

There are three macroscopic forms;[1]

A. Localized type is the most frequent type only affect to the rectum.

B. Segmentary type affecting only part of the left colon

C. Diffuse type affecting the complete colon.

Lesions of the same kind may also occur in the small intestine, where they are termed "enteritis cystica profunda"(ECP). The clinical history and endoscopic examination are insufficiency to diagnose so the Computed tomography and Magnetic resonance imaging may help.[2,7] Velenzuela el al[7] reported that the CT finding of the lesion at the rectum appeared as a non-infiltrating entity in the submucosa with loss of perirectal layers of fatty tissue and thickening of the levator ani muscle. By MRI, nodulation produced intense signals that increased T 2, illustrating the mucoprotein contents of cysts. Due to cystic rupture, they might present masses of mucin containing loose sheets of epithelial cells in the deep layers of bowel walls resulting misdiagnoses as a well-differentiated mucin-producing adenocarcinoma.[3] In this case, the computed tomographic finding revealed large ill-defined irregular low attenuation lesion at the posterior wall of the caecum and the ascending colon continuing with evidence of abscess formation at the right-side of the retroperitoneum. This finding could be either cystic rupture in colitis cystic profunda or mucinous adenocarcinoma of the colon. No evidence of colonic obstruction even large size and small size of the pericolic lymph nodes might be clues for CCP than mucinous adenocarcinoma.

CCP disorder is often associated with other disease that predispose to irritation of the bowel wall such as ulcerative colitis, Crohn's disease, Peutz-Jeghers syndrome, adenomatous polyps, dysentery and spastic colitis[8,9]. In this case, it associated with chronic active colitis.

Treatment includes bowel habit re-education and use of laxatives to reduce trauma and correct constipation.[1] Lesions have been shown to regress in 6-8 months when the constipation is prevented.[2] In the literature, it has reported that 43% of cases had local excision and only four cases underwent low anterior resection in order to treat the internal prolapsed.[2] It this case, due to large size causing

abdominal distension and misdiagnosis as mucinous adenocarcinoma of the colon, right half colectomy was performed.

In conclusion, colitis cystica profunda is a rare benign condition which can mimic mucinous adenocarcinoma of the colon. The awareness in diagnosis should prevent the patients form unnecessary surgery.

References

1. R. Higuera Alvarez, J. de la Pena Garcia, G.San Miguel, B. Castro. Colitis cystic profunda. Rev Esp Enefem Dig 2008;100:240-2.
2. E. Kayacetin, S. Kayacetin. Colitis cystica profunda simulating rectal carcinoma 2005;105:306-8.
3. S. Kruger, F. Noack, A.C. Feller, M. Birth. Colitis cystic profunda and giant inflammatory pseudopolyp in Crohn's disease 2005;20:383-4.
4. Kingsley B. Grant, Gilbert J. Roller. Colitis cystica Profunda ; A lesion of increasing significance to radiologists and pathologist ; Radiology 1967;89:110-1.
5. Gest CB, Reznick RK. Colitis cystica profunda. Review of the literature 1989;32(11):939-8.
6. Emad Qayed, Shanthi Srinivansan, Mohammmad Wehbi. A case of colitis cystica profunda in associated with diverticulitis : Am J Gastroenterol 2011;106:172-3.
7. Velenzuela M, Marthin-Ruiz JL, Alvarez-Cienfuegos E, Caballero AM, Gallego F, Rodriguez-Tellez M. Colitis cystica profunda: Imaging diagnosis and conservative treatment: reports of two cases. Dis colon rectum 1996;39(5): 587-90.
8. Zidi S. H., Marteau P., Piard F, Coffin B, Fure J. P., Ramboud J.C. Enterocolitis cystica profunda lesions in a patients with unclassified ucerature enterocolitis. Dig dis Sci 1994;34:426-32.
9. Magidson J. G, Lewin K. J. Diffuse colitis cystica profunda : reports of a case Am J Surg Pathol 1981;5: 393-5.
10. Strak W: Specimen septem hostorias et dissection dysentericom exhibens (thesis). Leiden, the Netherlands, 1766.
11. Virchow R: Die Krankhaften Geschwulste, vol 1. Berlin, Hirchwald, 1863.

THE ASEAN JOURNAL OF RADIOLOGY 2012: 18(3): 189-194 189

Case Report

A Case Report of Transmesenteric Hernia: CT Finding

Priyanut Phokhom

Department of radiology Bamrasnaradura Infectious Disease Institute Ministry of Public Health

Abstract

This is a case report of a rare computed tomography (CT) scan finding of transmesenteric internal herniation. The finding from CT scan first leaded to the diagnosis of left paraduodenal hernia. The right diagnosis was made during surgery. This report will suggest for the correct interpretation of CT scan for transmesenteric hernia.

Introduction

Internal hernias are a rare condition. The internal hernias involve protrusion of the viscera through the peritoneum or mesentery and into a compartment in the abdominal cavity. The conditions can be either congenital or acquired reasons. The incidence occurs around 1%-5.8% of all intestinal obstructions[1-3]. Internal hernias are divided into distinct subgroups based on the localizations; such as transmesenteric hernia, left and right paraduodenal hernias, transomental hernia, pericaecal hernia. The paraduodenal hernias are found in nearly half of the patients who have internal hernias[4].

Transmesenteric hernia is a rare cause of abdominal pain, account for 8% of all internal[5]. It can lead to bowel obstruction, ischemia and perforation with a high mortality. A timely and correct diagnosis with a rapid diagnostic tool is mandatory. However, clinical diagnosis of transmesenteric hernia is difficult for its nonspecific symptoms. This study presented a male patient of 66 years of age who developed transmesenteric hernias.

Case report

A 66-year-old obese Thai man came in with acute epigastric pain for 6 hours. He developed abdominal pain 1 day prior to arrive at Bumrasnaradura Infectious Disease Institute. He went to one government provincial hospital and was diagnosed as gastroenteritis. Six hours prior to arrived at hospital, his symptom got worse. He did not has any GI symptoms such as diarrhea or vomiting. He has underlying of benign prostatic hyperplasia. He is currently treated by alpha-blocker of his urinary symptom. He never has any abdominal surgery. On the physical examination, he had only epigastric tenderness with soft abdomen. He did not has inguinal hernia. Upon his laboratory work up, he had mild leukocytosis. Radiological studies were as followed;

Film acute abdomen: CXR PA upright view (Figure 1A) showed no obvious active cardiopulmonary lesion. Film abdomen supine view (Figure 1B) showed focal mild dilatation of small bowel loops at left upper abdomen. Soft tissue density was seen just below and overlying focal dilated bowel loops. Film abdomen upright view (Figure 1C) showed air-fluid level at peripheral part of focal dilatation of small bowel loops at left upper abdomen. Large soft tissue opacity in left upper to mid abdomen was seen obviously in this view. Then patient was sent to CT scan room to perform CT whole abdomen. CT scan showed clustered of dilated jejunal loops at left side of abdomen which superior portion of this bowel loops were located between posterior wall of stomach and anterior part of pancreatic body (Figure 2A). This finding looked similar to left paraduodenal hernia. The next lower axial slides (Figure 2B and 2C) showed cluster of dilated jejunal loops between lower part of posterior wall of stomach and anterior part pancreatic tail which left to superior mesenteric artery (SMA) and superior mesenteric vein (SMV). Stomach and transverse colon showed anterior displacement. However, mild engorged of SMA and SMV without displacement of these vessles were noted. Mild narrowing at distal part of jejunum was seen. Inward-distorted engorged mesenteric vessles to theses dilated bowel loops were detected at left lower abdomen (Figure 2D). Diagnosis by CT scan was suspected left paraduodenal hernia (PDH).

He was sent to operating room for abdominal

exploration. Operative finding showed defect lumen at mesentery of transverse colon and jejunal loops passed through mesenteric defect. No gangrene of dilated bowel loops was detected. Postoperative finding was diagnosed as transmesenteric internal hernia.

His symptom was improved as on second day after surgery. Then he came back home without complication. He was healthy at 1 month of follow up visit.

Discussion

Internal hernias are rare condition. The incidence accounts around 1%-5.8% of all intestinal obstructions[1-3,6]. Internal hernias are named according to the orifices they pass through. The most commonly seen internal hernias are as follows: left and right paraduodenal 53%, pericaecal 13%, transmesenteric 8%, intersigmoid 6%, supravesical and pelvis 6%, foramen Winslow 8% and transomental hernias 1-4%[5].

Transmesenteric hernia is intraperitoneal hernia which have no sac and consist of the protrusion of a loop of bowel through an aperture in the mesentery[7]. Transmesenteric hernia is a rare cause of small bowel obstruction and is seldom diagnosed preoperatively partly because of our unfamiliarity with this type of internal hernia. CT scan is recommended tool for diagnosis of internal hernias[8,9].

Preoperative diagnosis is difficult because of

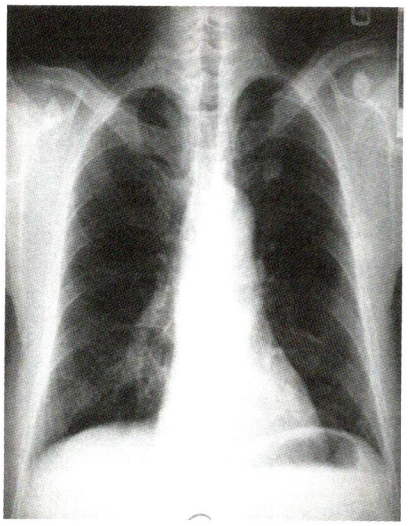

Figure 1A

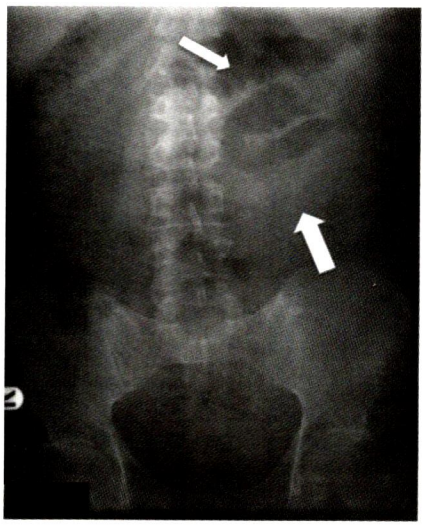

Figure 1B

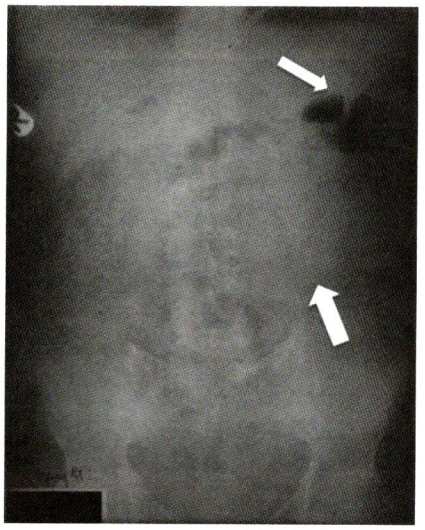

Figure 1C

Fig.1 Film acute abdomen series

A: Chest x-ray shows suboptimal study due to poor inspiration. However, no obvious cardiopulmonary abnormality is seen.

B: Film abdomen anteroposterior projection of abdomen supine view shows focal dilatation of small bowel loops (small arrow) at left upper abdomen and soft tissue density is seen just below and overlying focal bowel loops dilatation (large arrow).

C: Film abdomen anteroposterior projection of abdomen upright view shows air-fluid level at peripheral part of focal dilatation of small bowel loops at left upper abdomen (small arrow). Large soft tissue opacity in left upper to mid abdomen below focal bowel loops dilatation (large arrow) is shown.

clinical symptoms may range from mild intermittent digestive complaints to acute onset intestinal obstruction. If delayed in diagnosis may lead to serious complications such as strangulation or gangrene of bowel loops.

Imaging methods play an important role in the diagnosis of intestinal herniations. Plain X-rays is helpful in patient which presented with symptom of intestinal obstruction. Plain film can yield information regarding the intestinal segment from which

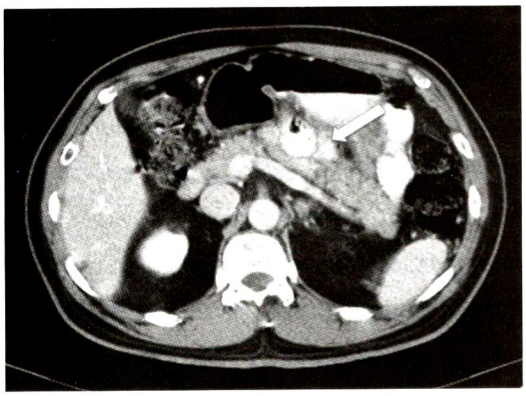

Figure 2A

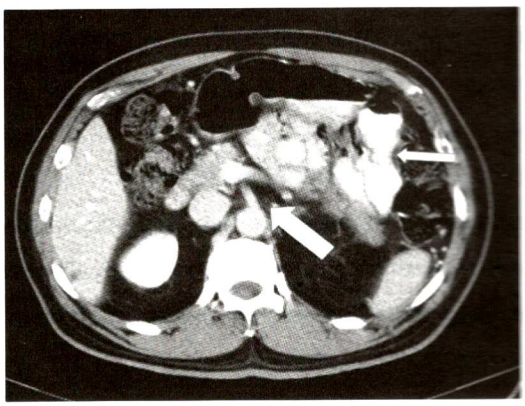

Figure 2B

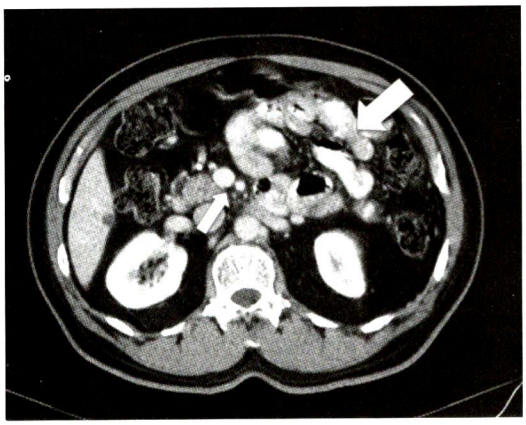

Figure 2C

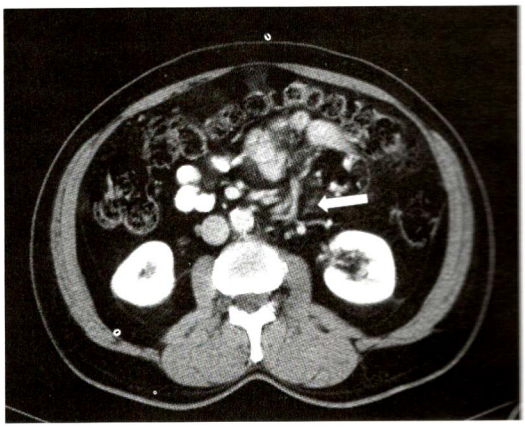

Figure 2D

Fig.2 Whole abdominal CT scan

A: Axial CT scan shows superior portion of cluster of dilated jejunal loops (arrow) locates between posterior wall of stomach and anterior part of pancreatic body. This finding looks similar to left paraduodenal hernia.

B: Axial CTscan lower to picture A at SMA origin (large arrow), shows cluster of dilated jejunal loops (small arrow) between lower part of posterior wall of stomach and anterior part of pancreatic tail.

C: Axial CT scan lower to picture B shows cluster of dilated jejunal loops (large arrow) which are located left sided to SMA and SMV (small arrow), but SMA and SMV are not change of location.

D: CT scan shows dilated and converging vessle of the mesenteric root(arrow) at left lower abdomen.

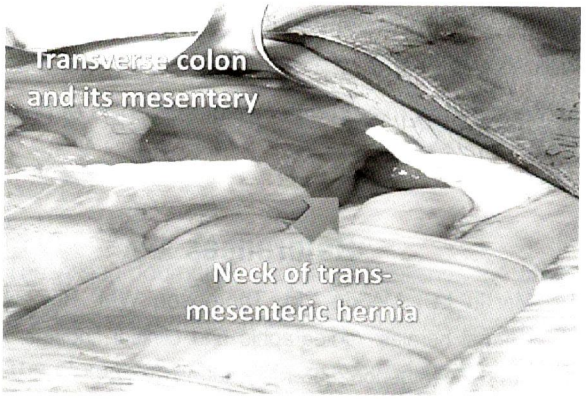

Figure 3A

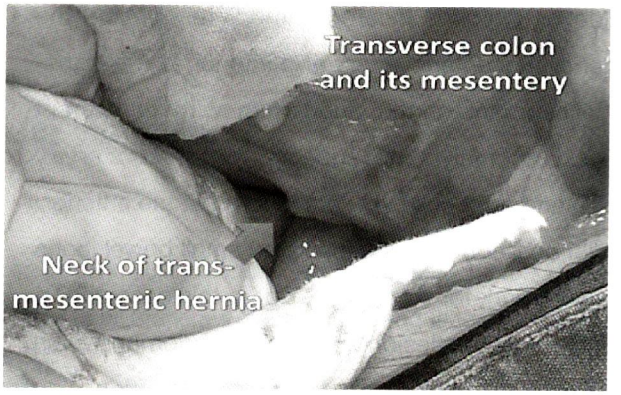

Figure 3B

Fig.3 Intra-operative finding of transmesenteric internal hernia.

the herniation stems and extension of the intestinal obstruction. But in early symptom of internal hernias CT scan is more better than plain film to show abnormal bowel loops such as dislocated, distended, expanded and cluster small intestinal segments. Moreover, CT scan also indicate dislocation of mesenteric vascular structures, fluid or free air in serious complications, which help surgeon for operative planning.

In our case report of transmenteric hernia, patient came to hospital with early symptom of gut obstruction then plain abdomen series and CT study showed very early finding of gut obstruction. In CT study showed mild dilatation of jejunal loops at left side abdomen, which superior portion of cluster of dilated small bowel loops were located between posterior wall of stomach and anterior part of pancreatic body which mimiced some findings of left paraduodenal hernia (PDH) causing misdiagnosis. Left PDH has incidence of approximately 40% of all internal hernias[1]. Left PDH develops through the fossa of Land-zert into the descending mesocolon and left of the transverse mesocolon and results from failure of fusion of the inferior mesentery to the parietal peritoneum[8]. CT finding of left PHD will show clustered dilated small-bowel loops between stomach and pancreas, behind pancreas itself or between transverse colon and left adrenal gland. There is usually mass effect that displaces the posterior wall of the stomach, the duodenal flexure inferiorly and the transverse colon inferiorly. The mesenteric vessels that supply the herniated small bowel segments are crowded, engorged and stretched at the entrance of the hernial sac. Because the anterior wall of the sac contains the inferior mesenteric vein (IMV) and left colic artery, CT demonstrates these vessels as a landmark above the encapsulated bowel loops[1,8]. In our case report, CT finding showed mild dilatation of jejunal loops between posterior wall of stomach and anterior surface of pancreas and anterior displacement of stomach and transverse colon, which mimiced left PDH. However, the main part of dilated bowel loop was located in left lower abdomen, which was confirmed by intraoperative finding as transmesenteric hernia.

In this case did not look like right paraduodenal hernia because right PDH involves the fossa of

Waldeyer, which is located immediately behind the superior mesenteric artery and inferior to the transverse segment of the duodenum with or without rotation anomaly. The superior mesenteric artery (SMA) and right colic vein are located at the anterior-medial border of the encapsulated small bowel loops as a landmark for right PDH[8]. But in this case shows mainly mass like lesion in left side abdomen which SMV and SMV are located in normal location.

Transmesenteric hernia is uncommon type of hernia about 8% of all internal hernia[5] and occurs in bimodal distribution, occurring in both pediatric and adult patients. In children, transmesenteric hernia is the most common type of internal hernia, occurring in 35% of this patient population. But in adult population, the cause is iatrogenic, usually related to prior abdominal surgery, especially with Roux-en-Y anastomosis, trauma or inflammation. Clinical and film finding may simulate a left PDH. CT finding shows dilated small bowel lateral to colon displaced omental fat with small bowel directly abutting abdominal wall. In this case showed no history of any surgery and it also very rare condition, then it may difficult to distinguish between transmenteric hernia and left PDH by finding study.

Conclusion

Transmesenteric internal hernia is one of the rare causes of small bowel obstruction. It should be in the differential diagnosis in patients with no prior abdominal surgery who frequently have recurrent clinical of gut obstruction. If image finding of patient look like left PDH, we will keep in mind, transmesenteric hernia may in differential diagnosis of patient.

References

1. Martin LC, Merkle EM, Thompson WM. Review of internal hernias: radiographic and clinical findings. AJR Am J Roentgenol 2006 Mar;186(3):703-17.
2. Lin CT, Hsu KF, Hong ZJ, Yu JC, Hsieh CB, Chan DC, et al. A paraduodenal hernia (Treitz's hernia) causing acute bowel obstruction. Rev Esp Enferm Dig Mar;102(3): 220-1.
3. Sen M, Inan A, Dener C, Bozer M. [Paraduodenal internal hernias: clinical analysis of two cases]. Ulus Travma Acil Cerrahi Derg 2007 Jul;13(3):232-6.
4. Virich G, Davies W. A massive left paraduodenal fossa hernia as an unusual cause of small bowel obstruction. Ann R Coll Surg Engl May;92(4):W7-9.
5. Takeyama N, Gokan T, Ohgiya Y, Satoh S, Hashizume T, Hataya K, et al. CT of internal hernias. Radiographics 2005 Jul-Aug;25(4):997-1015.
6. Hernandorena Gonzalez M, Dominguez MB, Munoz RD, Calaforra ST. [CT findings for internal paraduodenal hernias]. Radiologia 2009 Jul-Aug;51(4):444-5.
7. Janin Y, Stone AM, Wise L. Mesenteric hernia. Surg Gynecol Obstet 1980 May;150(5):747-54.
8. Blachar A, Federle MP, Dodson SF. Internal hernia: clinical and imaging findings in 17 patients with emphasis on CT criteria. Radiology 2001 Jan;218(1):68-74.
9. Blachar A, Federle MP, Brancatelli G, Peterson MS, Oliver JH, 3rd, Li W. Radiologist performance in the diagnosis of internal hernia by using specific CT findings with emphasis on transmesenteric hernia. Radiology 2001 Nov;221 (2):422-8.